

Carboxylate-Capped Analogues of Ru265 Are MCU Inhibitor Prodrugs

Nicholas P. Bigham, Zhouyang Huang,[§] Jesse Spivey,[§] Joshua J. Woods, Samantha N. MacMillan, and Justin J. Wilson*



Cite This: *Inorg. Chem.* 2022, 61, 17299–17312



Read Online

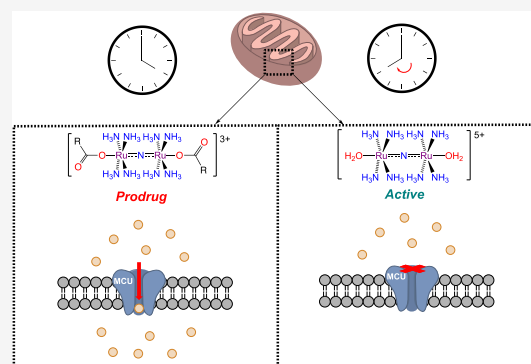
ACCESS |

Metrics & More

Article Recommendations

Supporting Information

ABSTRACT: The mitochondrial calcium uniporter (MCU) is a transmembrane protein that resides on the inner membrane of the mitochondria and mediates calcium uptake into this organelle. Given the critical role of mitochondrial calcium trafficking in cellular function, inhibitors of this channel have arisen as tools for studying the biological relevance of this process and as potential therapeutic agents. In this study, four new analogues of the previously reported Ru-based MCU inhibitor [ClRu(NH₃)₄(μ-N)Ru(NH₃)₄Cl]Cl₃ (Ru265) are reported. These compounds, which bear axial carboxylate ligands, are of the general formula [(RCO₂)Ru(NH₃)₄(μ-N)Ru(NH₃)₄(O₂CR)]X₃, where X = NO₃⁻ or CF₃SO₃⁻ and R = H (1), CH₃ (2), CH₂CH₃ (3), and (CH₂)₂CH₃ (4). These complexes were fully characterized by IR spectroscopy, NMR spectroscopy, and elemental analysis. X-ray crystal structures of 1 and 3 were obtained, revealing the expected presence of both the linear Ru(μ-N)Ru core and axial formate and propionate ligands. The axial carboxylate ligands of complexes 1–4 are displaced by water in buffered aqueous solution to give the aquated compound Ru265'. The kinetics of these processes were measured by ¹H NMR spectroscopy, revealing half-lives that span 5.9–9.9 h at 37 °C. Complex 1 with axial formate ligands underwent aquation approximately twice as fast as the other compounds. In vitro cytotoxicity and mitochondrial membrane potential measurements carried out in HeLa and HEK293T cells demonstrated that none of these four complexes negatively affects cell viability or mitochondrial function. The abilities of 1–4 to inhibit mitochondrial calcium uptake in permeabilized HEK293T cells were assessed and compared to that of Ru265. Fresh solutions of 1–4 are approximately 2-fold less potent than Ru265 with IC₅₀ values in the range of 14.7–19.1 nM. Preincubating 1–4 in aqueous buffers for longer time periods to allow for the aquation reactions to proceed increases their potency of mitochondrial uptake inhibition to match that of Ru265. This result indicates that 1–4 are aquation-activated prodrugs of Ru265'. Finally, 1–4 were shown to inhibit mitochondrial calcium uptake in intact, nonpermeabilized cells, revealing their value as tools and potential therapeutic agents for mitochondrial calcium-related disorders.



The kinetics of these processes were measured by ¹H NMR spectroscopy, revealing half-lives that span 5.9–9.9 h at 37 °C. Complex 1 with axial formate ligands underwent aquation approximately twice as fast as the other compounds. In vitro cytotoxicity and mitochondrial membrane potential measurements carried out in HeLa and HEK293T cells demonstrated that none of these four complexes negatively affects cell viability or mitochondrial function. The abilities of 1–4 to inhibit mitochondrial calcium uptake in permeabilized HEK293T cells were assessed and compared to that of Ru265. Fresh solutions of 1–4 are approximately 2-fold less potent than Ru265 with IC₅₀ values in the range of 14.7–19.1 nM. Preincubating 1–4 in aqueous buffers for longer time periods to allow for the aquation reactions to proceed increases their potency of mitochondrial uptake inhibition to match that of Ru265. This result indicates that 1–4 are aquation-activated prodrugs of Ru265'. Finally, 1–4 were shown to inhibit mitochondrial calcium uptake in intact, nonpermeabilized cells, revealing their value as tools and potential therapeutic agents for mitochondrial calcium-related disorders.

INTRODUCTION

The homeostasis and dynamics of intracellular calcium ions (Ca²⁺) are involved in a wide range of biological processes.^{1–3} Among the key organelles responsible for Ca²⁺ regulation are the mitochondria. Mitochondrial Ca²⁺ (*m*Ca²⁺) uptake is important for healthy cellular function, but dysregulation of this process can lead to deleterious effects. For example, *m*Ca²⁺ overload triggers cell death^{4,5} and has been implicated in a number of pathological conditions, including neurodegenerative disorders,^{6,7} heart disease,^{8–10} cancer,^{11,12} cystic fibrosis,^{13,14} and ischemia-reperfusion injury.^{15–17} Ca²⁺ influx into the mitochondria is mediated by the highly selective channel known as the mitochondrial calcium uniporter (MCU).^{18–22} This transmembrane protein resides in the inner mitochondrial membrane (IMM) as a tetrameric assembly comprising the primary Ca²⁺-transporting MCU subunit and the regulatory EMRE, MICU1, and MICU2 subunits.^{23–32} Given the role of *m*Ca²⁺ overload within various

diseases, inhibition of the MCU represents a promising therapeutic strategy.

To develop new therapeutic agents and tools for studying *m*Ca²⁺, extensive research efforts have been directed toward the identification of small-molecule MCU inhibitors.³³ To date, several organic^{34–40} and inorganic^{41–47} compounds have been discovered to possess MCU-inhibitory activity. Among these compounds, polynuclear Ru complexes are the oldest known MCU inhibitors, and recently developed analogues have shown promise for this application. The earliest inhibitor of this type identified is the trinuclear oxo-bridged complex ruthenium red

Received: August 15, 2022

Published: October 19, 2022

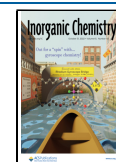
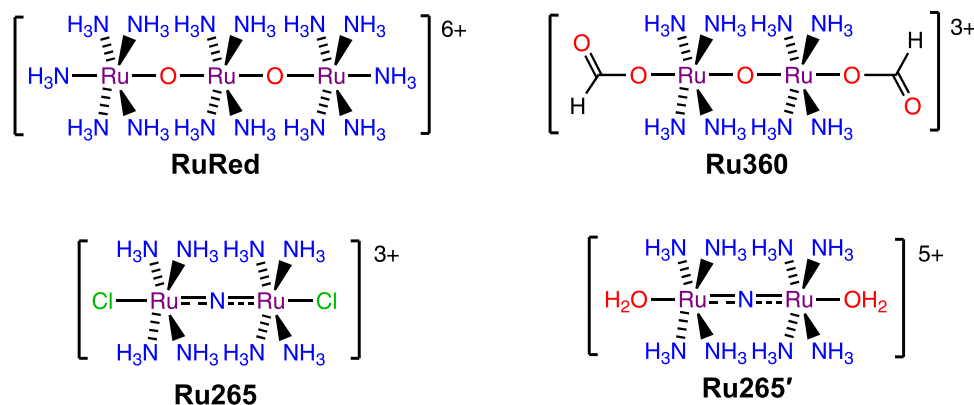


Chart 1. Structures of Ru-Based MCU Inhibitors



Scheme 1. Strategy to Develop Prodrugs for Ru265' through Aquation of the Axial Ligands

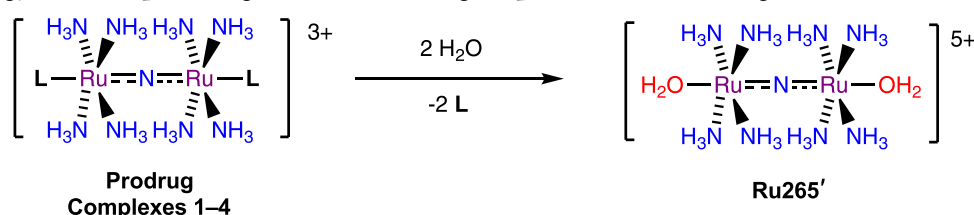
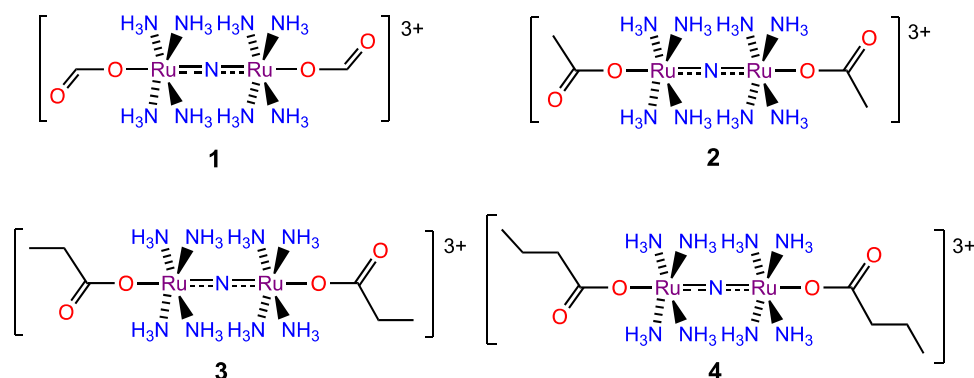


Chart 2. Structures of Compounds Discussed in This Work

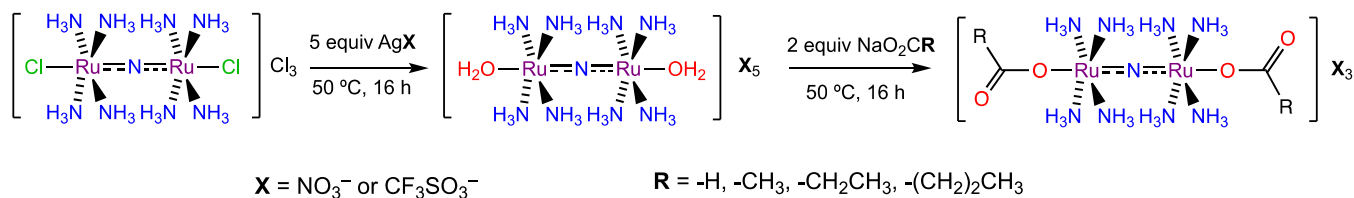


(RuRed; Chart 1), which was originally applied as a cytological stain.⁴⁸ Subsequent studies, however, indicated that an impurity present within RuRed samples was responsible for the *m*-Ca²⁺ uptake-inhibitory activity.^{41,49} These efforts ultimately led to the discovery of the dinuclear oxo-bridged complex Ru360 (Chart 1).^{41,42,50} This complex exhibits nM potency as an MCU inhibitor in isolated mitochondria and permeabilized cells.^{42,44} Its use in intact cell systems, however, has yielded inconsistent results—a possible consequence of its poor cell permeability and redox instability.⁵¹

Recently, an analogue of Ru360 called Ru265 was reported (Chart 1).⁴⁵ This compound is structurally similar to Ru360 but contains a bridging nitrido (N³⁻) rather than an oxo (O²⁻) ligand. In addition, the Ru centers in Ru265 are both in the +4 oxidation state, whereas Ru360 is a mixed valent Ru³⁺/Ru⁴⁺ species. Notably, this relatively simple modification confers Ru265 with enhanced redox stability and the ability to inhibit *m*-Ca²⁺ uptake in intact, nonpermeabilized cells. These properties have been leveraged to elicit therapeutic effects in both *in vitro* and *in vivo* models of ischemic stroke.⁵² The axial chloride ligands of Ru265 aquate on the order of minutes

under physiological conditions, indicating that the active inhibitor is the diaqua-capped species Ru265' (Chart 1). Accordingly, mutagenesis studies and molecular docking studies on the DIME region of the MCU, a highly conserved amino acid residue sequence that resides near the pore opening, revealed Ru265' to bind at this site.⁴⁶

Given that the axial chloride ligands of Ru265 rapidly dissociate and that the resulting Ru265' is an active MCU inhibitor, we postulated that modifications to the axial sites of this compound class could afford an approach to develop prodrugs that possess improved properties for different biological applications (Scheme 1). Specifically, the implementation of less labile axial ligands would yield compounds whose pharmacokinetic, cellular uptake, and targeting properties could be optimized. In an initial effort toward these goals, we present in this study an investigation of alkyl carboxylates as suitable candidates for developing aquation-activated Ru265' prodrugs. Four new derivatives of Ru265, bearing alkyl carboxylates of different carbon chain lengths as axial ligands, were synthesized and characterized (Chart 2). Encouragingly, the aquation kinetics of these complexes are substantially

Scheme 2. Synthetic Scheme for Compounds 1, 2, 3, and 4^a

^aCompounds 1, 2, and 3 were synthesized as nitrate salts, whereas compound 4 was synthesized as a triflate salt.

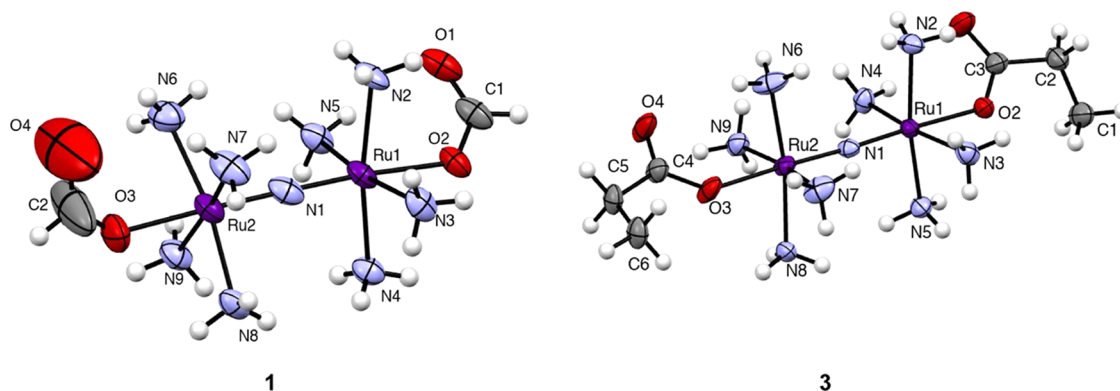


Figure 1. Crystal structures of 1 and 3. Outer-sphere ions and solvent molecules are omitted for clarity. Thermal ellipsoids are shown at the 50% probability level. For 1, only one of the two complex cations present in the asymmetric unit is shown. The other complex cation is shown in Figure S26 in the SI. Crystallographic information for both complexes is given in Table 1. Interatomic distances and angles are given in Table 2 and Table S1.

slower than those of Ru265, a property that can be leveraged for a time-dependent increase in MCU-inhibitory activity. Through a series of cell biology studies, this work highlights the potential use of axial carboxylate ligands for the development of Ru265' prodrugs through ligand dissociation.

RESULTS AND DISCUSSION

Synthesis and Characterization. To explore the potential of oxygen donors as axial ligands for Ru265' prodrugs, the smallest carbon chain carboxylates, formate, acetate, propionate, and butyrate, were investigated. The fact that Ru360 is isolated as the formate-capped species⁴¹ and that recent two-dimensional (2D) [¹H,¹⁵N] heteronuclear single quantum coherence nuclear magnetic resonance (HSQC NMR) spectroscopic studies on ¹⁵N-labeled Ru265 show this compound to covalently interact with aspartate and glutamate⁵³ demonstrates the viability of employing carboxylates as axial ligands for these dinuclear ruthenium complexes. Our choice of using these four carboxylates for these initial studies was motivated by the expected sequential enhancement in complex lipophilicity afforded by the systematic increase in carbon chain length. The calculated log *P* values for these carboxylic acids are −0.54, −0.28, 0.33, and 0.79 for formic, acetic, propanoic, and butyric acids, respectively, reflecting the magnitudes of increases in lipophilicity expected for the complexes. Cellular uptake is often correlated to lipophilicity,^{54–61} and metal complexes bearing lipophilic groups have leveraged this property to enhance their therapeutic potentials.^{62–67} We postulated that the use of these ligands could allow us to investigate this relationship for these Ru-based MCU inhibitors.

The general two-step syntheses required to access the formate (1), acetate (2), propionate (3), and butyrate (4) complexes are presented in Scheme 2. The reaction

commenced from Ru265 by the addition of 5 equiv of either silver nitrate (1–3) or silver trifluoromethanesulfonate (triflate) (4) at 50 °C for 16 h in water to remove both the inner- and outer-sphere chlorides as insoluble silver chloride. The resulting aqueous solution of Ru265' was then treated with 2 equiv of the sodium salt of the desired carboxylate to coordinate to the metal center in place of the coordinated water molecules and allowed to heat at 50 °C for 16 h. This temperature and reaction time were chosen to maximize product yield while preventing decomposition of the Ru(μ -N)Ru core, which can occur at higher temperatures. The nitrate salts of 1–3 were crystallized by the vapor diffusion of *p*-dioxane into an aqueous solution of the compounds containing 10% of their corresponding carboxylic acid to prevent aquation. For the triflate salt 4, vapor diffusion of diethyl ether into a methanolic solution of the crude compound afforded analytically pure material.

The infrared (IR) spectra of 1–4 (Figures S1–S4, Supporting Information, SI) show diagnostic features that are consistent within their proposed structures. For 1–3, an intense peak at 1383 cm^{−1}, which is the characteristic energy of the nitrate counterion stretching mode, is present. Within the IR spectrum of compound 4, peaks diagnostic of the triflate counterion at 1269, 1223, 1145, and 637 cm^{−1} are observed.⁶⁸ The four complexes all give rise to intense peaks near 3400, 1600, and 1400 cm^{−1}, which arise from the N–H stretching modes of the ammine ligands and the symmetric and asymmetric C–O stretches of the carboxylates, respectively. Another key vibrational mode that is characteristic of these complexes is the asymmetric Ru–N–Ru stretch. For 2–4, this mode is observed at 1039, 1040, and 1037 cm^{−1}, respectively. For 1, this mode occurs at a slightly higher energy of 1064 cm^{−1}. The higher energy of the Ru–N–Ru stretch of 1 correlates with the lower basicity and weaker donor strength of

the axial formate ligand compared to the alkyl carboxylates in 2–4.

All four complexes give rise to well-resolved ^1H NMR spectra, consistent with their diamagnetic ground states (Figures S5–S8, SI), that show characteristic resonances from both the equatorial ammine ligands and the axial carboxylates. The ^1H NMR resonance in DMSO- d_6 of the ammine ligands for all four complexes is apparent as a broad singlet near 3.95 ppm. For comparison, the chemical shift for the amines of Ru265 resides further downfield at 4.15 ppm.⁴⁵ In the aqua-capped analogue Ru265', however, the peak appears at 3.96 ppm (Figure S9, SI), like those observed for 1–4. Thus, axial oxygen donors induce a small shielding effect on the protons of the ammine ligand, as has been shown previously.⁵³ Similarly, the ^1H resonances of the carboxylates are also shifted upfield by approximately 0.2 ppm relative to the free ligands. Further characterization by $^{13}\text{C}\{^1\text{H}\}$ (Figures S10–S13, SI) and ^{19}F (Figure S14, SI) NMR spectroscopy of the complexes reveals the expected peaks for carboxylate ligands and the presence of the triflate counterion for 4.

X-ray Crystallography. Via the crystallization methods described above, single crystals of 3 suitable for X-ray diffraction were obtained. To grow X-ray diffraction-quality crystals of 1, it was first prepared as the triflate salt and then crystallized by the vapor diffusion of diethyl ether into a solution of it in methanol. The resulting crystal structures are shown in Figure 1, crystallographic data collection parameters and refinement statistics are given in Table 1, and selected

interatomic distances and angles are collected in Table 2. Notably, the asymmetric unit of 1 contains two molecules that are nearly identical. For simplicity, the structural data of just one of these molecules are tabulated in Table 2. Data for the second molecule in the asymmetric unit are presented in the SI (Table S1 and Figure S26, SI).

Both crystal structures reveal the linear Ru(μ -N)Ru core to remain intact with the equatorial positions completed by the NH_3 ligands and the axial positions occupied by the corresponding carboxylates. The linearity of this motif is reflected by the Ru–N–Ru angles of 176.5(5) and 175.43(19)° for 1 and 3, respectively. In addition, the Ru–N distances of the bridging nitrido range from 1.745(3) to 1.756(9) Å in 1 and 3. These values are notably shorter than the Ru–N distances for the equatorial NH_3 ligands, which span 2.089(3) Å to 2.122(7) Å. The shorter Ru–N distance of the bridging nitrido is consistent with the multiple bonding character of this interaction. These values are similar to those of both Ru265 and Ru265', for which the bridging Ru–N distances are 1.7421(7)⁴⁵ and 1.73871(15) Å,⁵¹ respectively. The axial Ru–O distances differ between 1 and 3. For 3, the Ru–O interatomic distances are 2.076(2) and 2.082(3) Å, whereas for 1, they are on average slightly greater, ranging from 2.080(8) to 2.110(6) Å. Bond distance differences are considered significant if the difference is more than 3 times the standard uncertainty of their difference.⁶⁹ The average Ru–O bond distances of 1 are significantly different compared to the average Ru–O bond distances of 3, given that their difference is 4 times the standard uncertainty of their differences. The longer distances within 1 may be a consequence of the weaker donor strength of formate compared to propionate, a property that is also reflected by the smaller pK_a of formic acid. Notably, for both complexes, these Ru–O distances are slightly shorter than those found in mononuclear Ru-carboxylate compounds, which typically fall within 2.00–2.200 Å.^{70–74} These axial distances are longer, however, than the Ru–O interactions found within the crystal structure of the formate-capped Ru360, which is 2.033(3) Å.⁴¹ The longer Ru–O axial distances found within 1 and 3 may be a consequence of the larger trans influence of the bridging nitrido present within these complexes compared to the bridging oxo ligand found in Ru360. The arrangement of the eight equatorial ammine ligands on each Ru center is staggered for 1 but eclipsed for 3. Notably, within the structures of Ru265 and Ru265', the ammine ligands are arranged in an eclipsed configuration. From an electronic and molecular orbital perspective, the eclipsed conformation is not required. This fact is reflected within the crystal structure of the ethylenediamine analogue of Ru265, which attains a staggered conformation.⁴⁵ Whether these complexes attain staggered versus eclipsed conformations is most likely a consequence of solid-state packing interactions. Finally, intramolecular hydrogen-bonding interactions between the carboxylate and ammine ligands are present within both 1 and 3. These interactions are similar to those frequently observed within carboxylate- or carbamate-bearing Pt^{4+} ammine complexes that have been used as prodrugs for cisplatin.^{62,75}

Kinetics of Axial Carboxylate Dissociation via NMR Spectroscopy. With the carboxylate compounds 1–4 fully characterized, we sought to investigate their aquation kinetics. As previously noted, the axial chloride ligands of Ru265 are substituted by water within minutes under physiologically relevant conditions.⁵¹ Thus, the viability of 1–4 as prodrugs

Table 1. X-ray Crystal Data and Structure Refinement Details for 1 and 3

compound	1·3MeOH	3·H ₂ O
empirical formula	C ₆ H ₂₉ F ₉ N ₉ O ₁₄ Ru ₂ S ₃	C ₆ H ₃₆ N ₁₂ O ₁₄ Ru ₂
formula weight	920.70	702.57
<i>a</i> (Å)	25.0552(2)	10.41150(10)
<i>b</i> (Å)	10.35730(10)	12.02830(10)
<i>c</i> (Å)	24.9114(3)	20.3198(2)
α (deg)	90	90
β (deg)	100.8730(10)	104.6280(10)
γ (deg)	90	90
<i>V</i> (Å ³)	6348.56(11)	2462.22(4)
<i>Z</i>	8	4
crystal system	monoclinic	monoclinic
space group	<i>P</i> 2 ₁ / <i>c</i>	<i>P</i> 2 ₁ / <i>n</i>
ρ_{calcd} (Mg m ⁻³)	1.927	1.895
μ (Cu <i>K</i> α), mm ^{-1a}	10.681	
μ (Mo <i>K</i> α), mm ^{-1a}		1.310
λ , Å	1.54184	0.7073
<i>T</i> (K)	100.0(8)	100.00(10)
2 θ range (deg)	3.593–77.525	2.072–26.022
independent reflections	27170	4846
<i>R</i> _{int}	0.079	0.0286
number of parameters	795	482
largest diff. peak and hole (Å ⁻³)	2.203/–2.018	1.717/–0.737
GoF ^c	1.041	1.165
<i>R</i> ₁ / <i>wR</i> ² (all data) ^b	0.0896/0.2330	0.0343/0.0866
<i>R</i> ₁ / <i>wR</i> ² (<i>I</i> > 2 σ) ^b	0.0820/0.2260	0.0333/0.0860

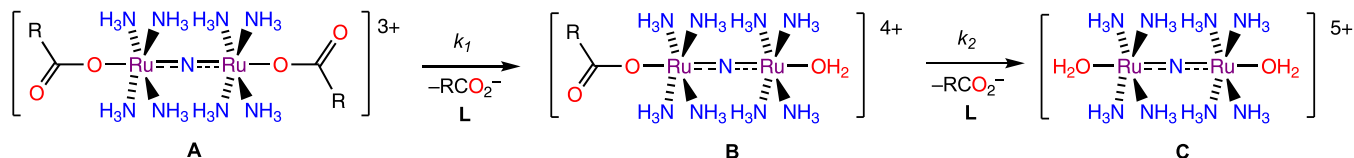
^aCu *K* α λ = 1.54184 Å; Mo *K* α λ = 0.7073 Å. ^b $R_1 = \sum |F_o| - |F_c| / \sum |F_o|$; $wR^2 = \{ \sum [w(F_o^2 - F_c^2)^2] / \sum (F_o^2)^2 \}^{1/2}$. ^cGoF = $\{ \sum [w(F_o^2 - F_c^2)^2] / (n - p) \}^{1/2}$, where *n* is the number of data and *p* is the number of refined parameters.

Table 2. Selected Interatomic Distances and Angles for 1 and 3^{a,b}

selected interatomic distances (Å) for 1·3MeOH				selected interatomic distances (Å) for 3·H ₂ O			
Ru(1)–O(2)	2.110(6)	Ru(2)–O(3)	2.080(8)	Ru(1)–O(2)	2.076(2)	Ru(2)–O(3)	2.082(3)
Ru(1)–N(1)	1.756(9)	Ru(2)–N(1)	1.730(9)	Ru(1)–N(1)	1.745(3)	Ru(2)–N(1)	1.743(3)
Ru(1)–N(2)	2.105(7)	Ru(2)–N(6)	2.117(9)	Ru(1)–N(2)	2.119(3)	Ru(2)–N(6)	2.114(3)
Ru(1)–N(3)	2.110(7)	Ru(2)–N(7)	2.122(8)	Ru(1)–N(3)	2.115(3)	Ru(2)–N(7)	2.115(4)
Ru(1)–N(4)	2.107(8)	Ru(2)–N(8)	2.107(8)	Ru(1)–N(4)	2.089(3)	Ru(2)–N(8)	2.100(3)
Ru(1)–N(5)	2.122(7)	Ru(2)–N(9)	2.117(8)	Ru(1)–N(5)	2.096(3)	Ru(2)–N(9)	2.098(3)
selected interatomic angles (deg) for 1				selected interatomic angles (deg) for 3			
N(1)–Ru(1)–O(2)	175.9(3)	N(1)–Ru(2)–O(3)	176.0(4)	N(1)–Ru(1)–O(2)	177.49(12)	N(1)–Ru(2)–O(3)	177.65(12)
N(1)–Ru(1)–N(2)	96.1(4)	N(1)–Ru(2)–N(6)	94.6(4)	N(1)–Ru(1)–N(2)	95.28(12)	N(1)–Ru(2)–N(6)	94.64(14)
N(1)–Ru(1)–N(3)	95.0(3)	N(1)–Ru(2)–N(7)	96.0(4)	N(1)–Ru(1)–N(3)	95.96(13)	N(1)–Ru(2)–N(7)	96.57(14)
N(1)–Ru(1)–N(4)	93.4(3)	N(1)–Ru(2)–N(8)	96.0(4)	N(1)–Ru(1)–N(4)	93.08(13)	N(1)–Ru(2)–N(8)	95.27(12)
N(1)–Ru(1)–N(5)	93.8(3)	N(1)–Ru(2)–N(9)	92.3(3)	N(1)–Ru(1)–N(5)	95.09(12)	N(1)–Ru(2)–N(9)	92.64(13)
N(2)–Ru(1)–N(3)	87.3(3)	N(6)–Ru(2)–N(7)	89.7(4)	N(2)–Ru(1)–N(3)	89.92(13)	N(6)–Ru(2)–N(7)	89.33(14)
N(2)–Ru(1)–N(4)	170.4(3)	N(6)–Ru(2)–N(8)	169.5(4)	N(2)–Ru(1)–N(4)	89.95(13)	N(6)–Ru(2)–N(8)	170.05(14)
N(2)–Ru(1)–N(5)	90.0(3)	N(6)–Ru(2)–N(9)	91.4(4)	N(2)–Ru(1)–N(5)	169.61(12)	N(6)–Ru(2)–N(9)	89.48(14)
N(2)–Ru(1)–O(2)	87.2(3)	N(6)–Ru(2)–O(3)	85.9(4)	N(2)–Ru(1)–O(2)	86.50(11)	N(6)–Ru(2)–O(3)	87.40(14)
N(3)–Ru(1)–N(4)	90.7(3)	N(7)–Ru(2)–N(8)	89.8(4)	N(3)–Ru(1)–N(4)	170.94(12)	N(7)–Ru(2)–N(8)	88.62(13)
N(3)–Ru(1)–N(5)	171.0(3)	N(7)–Ru(2)–N(9)	171.6(4)	N(3)–Ru(1)–N(5)	89.51(12)	N(7)–Ru(2)–N(9)	170.78(13)
N(3)–Ru(1)–O(2)	82.8(3)	N(7)–Ru(2)–O(3)	88.0(4)	N(3)–Ru(1)–O(2)	82.25(11)	N(7)–Ru(2)–O(3)	82.27(13)
N(4)–Ru(1)–N(5)	90.6(3)	N(8)–Ru(2)–N(9)	87.6(3)	N(4)–Ru(1)–N(5)	88.99(12)	N(8)–Ru(2)–N(9)	90.98(13)
N(4)–Ru(1)–O(2)	83.2(3)	N(8)–Ru(2)–O(3)	83.5(4)	N(4)–Ru(1)–O(2)	88.70(11)	N(8)–Ru(2)–O(3)	82.68(12)
N(5)–Ru(1)–O(2)	88.5(3)	N(9)–Ru(2)–O(3)	83.7(4)	N(5)–Ru(1)–O(2)	83.15(11)	N(9)–Ru(2)–O(3)	88.53(12)
Ru(1)–N(1)–Ru(2)	176.5(5)			Ru(1)–N(1)–Ru(2)	175.43(19)		

^aAtoms are labeled as shown in Figure 1. Values in parentheses indicate the standard uncertainty in the last significant figure. ^bCompound 1 contains two molecules in the asymmetric unit. Data shown are from one of these two molecules. Interatomic distances and angles are similar between the two molecules. Data for the second molecule are shown in the SI (Table S1 and Figure S26).

Scheme 3. Aquation Pathway of the Carboxylate-Functionalized Compounds



for Ru265' would require them exhibit substantially slower rates of aquation. To assess these properties, the complexes were incubated in pH 7.4 3-morpholinopropane-1-sulfonic acid (MOPS) buffered solution at 37 °C and monitored by ¹H NMR spectroscopy to follow the dissociation of the axial ligands over time. All complexes (A) underwent a sequential ligand substitution reaction with water to yield Ru265' (C) via a detectable mono-aquated intermediate B, as shown in Scheme 3.

As the aquation reactions progressed, resonances arising from the free ligand (L) and mono-aquated species B arose, concomitant with the decay of the intact complex A, as shown in Figure 2a for 1 and Figures S15–S17 (SI) for 2–4. Their relative concentrations were determined by integrating the peaks of their ¹H NMR signals. Rate constants for both the first (k_1) and second (k_2) aquation steps were calculated by fitting the concentration vs time data to the established integrated rate laws for consecutive $A \rightarrow B \rightarrow C$ kinetic process (eqs 1–4).⁷⁶ A representative data analysis for 1 is shown in Figure 2b. For 1, the relative concentration of Ru265' (C), which is not directly observable by ¹H NMR spectroscopy in D₂O, was calculated using mass balance (eq 5). For 2–4, the ¹H NMR signals of A and B, overlap, thus requiring analysis using the sum of the concentrations of these

species. The kinetics data for all four compounds are given in Table 3.

$$[A]_t = [A]_0 \exp(-k_1 t) \quad (1)$$

$$[B]_t = [B]_0 \exp(-k_2 t) + [A]_0 k_1 (k_2 - k_1)^{-1} \{ \exp(-k_1 t) - \exp(-k_2 t) \} \quad (2)$$

$$[C]_t = [C]_0 + [B]_0 \{ 1 - \exp(-k_2 t) \} + [A]_0 (1 + \{ k_1 \exp(-k_2 t) - k_2 \exp(-k_1 t) \} / (k_2 - k_1)) \quad (3)$$

$$[L]_t = [B]_t + 2[C]_t \quad (4)$$

$$[A]_t + [B]_t + [C]_t = 400 \mu\text{M} \quad (5)$$

For all four complexes, k_1 was measured to be approximately an order of magnitude smaller than k_2 . Thus, aquation of these carboxylate complexes is rate-limited by the dissociation of the first ligand. This result is comparable to Ru265, for which aquation of the first chloride ligand is also an order of magnitude smaller than that of the second.⁵³ The half-lives of carboxylate ligand dissociation among the four complexes are on the order of hours. For comparison, the axial chloride ligands of Ru265 undergo aquation with a half-life of

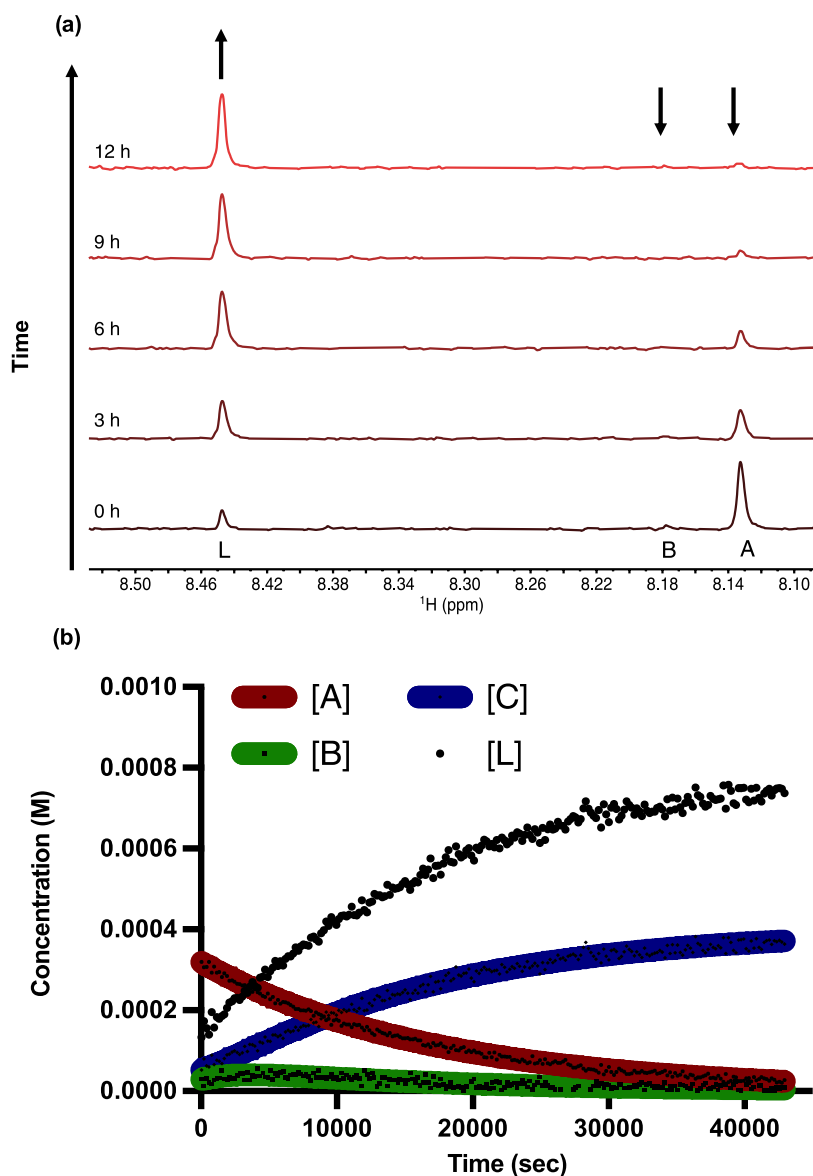


Figure 2. Representative kinetic analysis of **1** at 37 °C via ¹H NMR spectroscopy in pH 7.4 MOPS-buffered solution containing 10% D₂O and <1% *p*-dioxane as a chemical shift reference. (a) Proton resonances of each species A, B, and L are shown, and (b) the relative concentration of each species is plotted over time to calculate the rate constants k_1 and k_2 . Analyses for **2**, **3**, and **4** can be found in the SI (Figures S15–S17).

Table 3. Aquation Rate Constants (k_1 and k_2) and Half-Lives ($t_{1/2}$) of Ru265 and Compounds 1–4 at 37 °C^a

complex	$k_1 \times 10^5$ (s ⁻¹)	$t_{1/2(1)}$ (h)	$k_2 \times 10^4$ (s ⁻¹)	$t_{1/2(2)}$ (h)	pK _a (HL)
Ru265 ^b	49.2	0.038			−5.90
1	5.9 ± 0.2	3.3 ± 0.1	3.6 ± 0.3	0.50 ± 0.05	3.75
2	2.0 ± 0.5	9.9 ± 2.4	3.0 ± 1.2	0.7 ± 0.3	4.75
3	2.8 ± 0.1	6.9 ± 0.2	3.3 ± 0.5	0.6 ± 0.1	4.88
4	3.2 ± 0.1	5.9 ± 0.2	2.8 ± 0.2	0.700 ± 0.004	4.82

^aThe pK_a values of the conjugate acid of the free ligands are also given. ^bRef 51. The rate constant was determined using UV–vis spectroscopy and was only able to resolve the first aquation step.

approximately 2 min under these same conditions.⁵¹ Thus, the prolonged lifetime of the carboxylate-capped compounds portends to their potential use as prodrugs for Ru265'. In comparing the rate constants between compounds 1–4, those of **1** are 2–3 times greater than those of 2–4. The pK_a value of formic acid, the conjugate acid of the carboxylate ligand within **1**, is an order of magnitude smaller than the other alkyl carboxylates employed within 2–4. Thus, the faster aquation

rate of **1** correlates with the poorer basicity and donor strength of formate. Furthermore, as noted above in our discussion of the X-ray crystal structures, the interatomic axial Ru–O distances within **1** are longer than those found in **3**. Thus, ground state destabilization of **1** due to weaker Ru–O interactions appears to give rise to the faster dissociation rates observed within this complex. Collectively, these results demonstrate that axial position inertness of Ru265 analogues

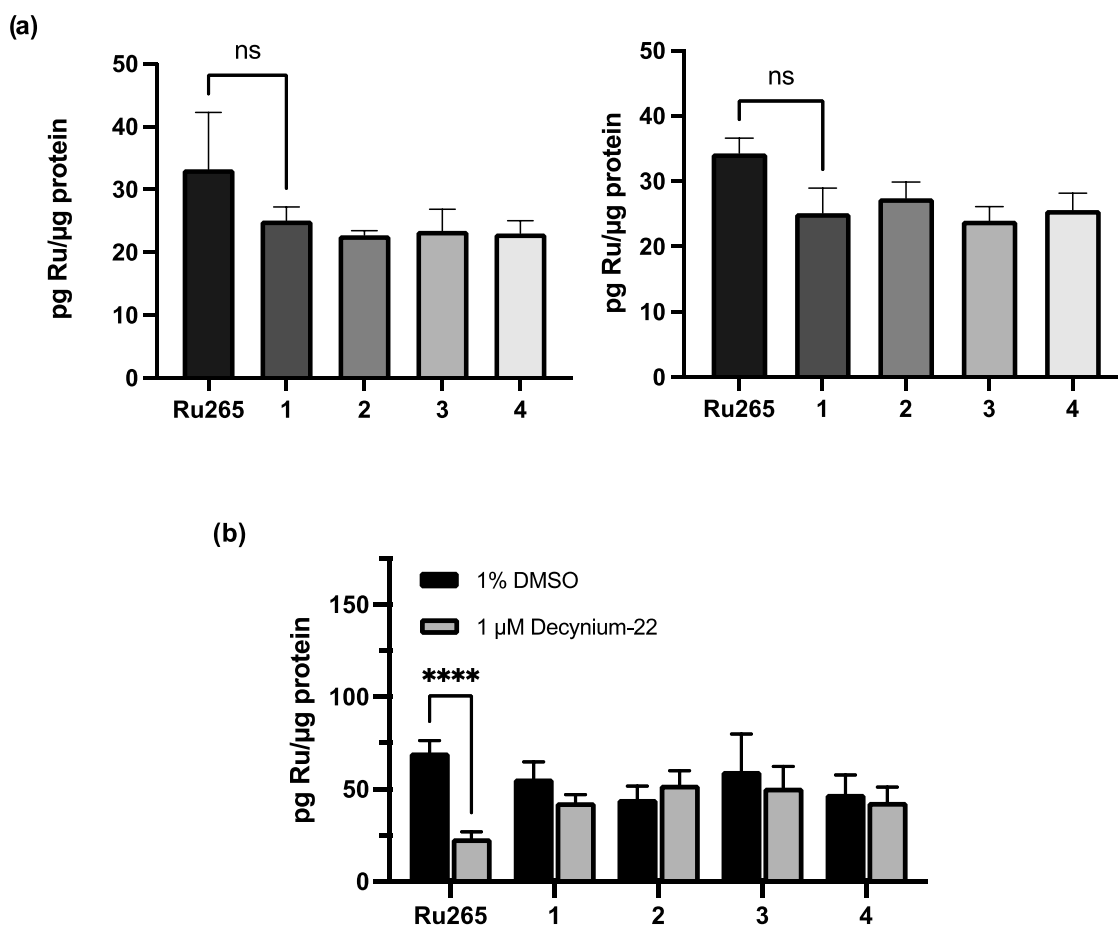


Figure 3. (a) Cellular uptake of Ru265, 1, 2, 3, and 4 in HeLa (left) and HEK293T (right) cells after incubating the cells with 50 μM of the compound for 2 h. (b) Cellular uptake of Ru265, 1, 2, 3, and 4 in HeLa cells in the presence and absence of the OCT3 inhibitor decynium-22 after incubating the cells with 50 μM of the compound for 3 h. Data are represented as the mean uptake \pm standard deviation (SD); **** p < 0.005; ns = not significant; n = 3.

can be systematically tuned via the use of ligands of different donor strengths.

Cytotoxicity and Cellular Uptake. The key properties of Ru265 that make it valuable as an MCU inhibitor are its limited cytotoxicity and its ability to permeate the cell membrane, a feature that most likely arises from its high redox stability.⁵¹ To assess the suitability of 1–4 in these contexts, we evaluated their cytotoxic effects and cellular uptake in both HeLa and HEK293T cells. The cytotoxicity of each complex was determined using the colorimetric thiazolyl blue tetrazolium bromide (MTT) assay. With 72 h incubation periods, the cell viability of both cell lines remained greater than 90% at concentrations up to 100 μM (Figures S18 and S19, SI). In addition, the JC-1 assay was used to verify that complexes 1–4 did not perturb the mitochondrial membrane potential of either cell line when administered at 50 μM for 24 h (Figures S20–S22, SI). Having shown that 1–4 do not negatively affect cell viability or mitochondrial function, their cellular uptakes were next determined. Freshly thawed stock solutions of the four compounds as well as Ru265 were incubated at 50 μM for 2 h with both HeLa and HEK293T cells, and their intracellular accumulation was quantified by graphite furnace atomic absorption spectroscopy (GFAAS). As shown in Figure 3a, all four complexes and Ru265 are taken up by both cell lines to a similar extent. Thus, the presence of these different carboxylate ligands does not influence cellular

uptake. This observation argues against a passive uptake mechanism for which increasing lipophilicity should correlate with enhanced cellular uptake.^{54–56,58} We have previously reported that Ru265 enters cells through the organic cation transporter 3 (OCT3).⁵¹ This transporter is upregulated in many tissues, including liver, heart, and skeletal muscle,^{77,78} and facilitates the entry of organic cationic species like histamine, choline, dopamine, and norepinephrine.^{79,80} To determine if 1–4 may similarly be substrates for the OCT3, their uptake in HeLa cells in the presence of the OCT3-specific inhibitor 1,1'-diethyl-2,2'-cyanine iodide (decynium-22) was determined. As shown in Figure 3b, only the uptake of Ru265 was diminished in the presence of the OCT3 inhibitor. These results suggest that OCT3 only mediates the uptake of Ru265 and not those of the carboxylate-capped analogues. Furthermore, these results also indicate that the carboxylate-capped species are entering cells in their intact forms, prior to aquation. After aquation, uptake of the resulting Ru265' would be diminished in the presence of the OCT3 inhibitor.

Mitochondrial Ca^{2+} Uptake Inhibition in Permeabilized Cells. Given the favorable cellular uptake and lack of cytotoxicity of 1–4, their MCU-inhibitory properties in digitonin-permeabilized HEK293T cells were investigated following established protocols.⁸¹ In the presence of freshly prepared 1 μM solutions of either Ru265 or 1–4, complete abrogation of $_{m}\text{Ca}^{2+}$ uptake was observed in these permeabi-

lized cells. The administered concentrations for each compound were varied to obtain dose–response curves for MCU inhibition from which 50% inhibitory concentration (IC_{50}) values were determined (Figures S23 and S24, SI). All four complexes exhibit nanomolar potency but are approximately 2-fold less active than Ru265 (Table 4).

Table 4. IC_{50} Values of MCU-Mediated mCa^{2+} Uptake Inhibition for Ru265 and Derivatives in Permeabilized HEK293T Cells (1×10^7 Cells/mL)

complex	IC_{50} (nM)
Ru265 ^a	8.6 ± 2.2
1	14.7 ± 2.9
2	18.8 ± 1.2
3	19.1 ± 1.7
4	18.7 ± 0.1

^aRef 46.

Although 1–4 are slightly less potent than Ru265, their ability to aquate within the hour timescale to yield Ru265' prompted us to investigate their time-dependent MCU-inhibitory properties. Before assessing MCU inhibition in permeabilized HEK293T cells, each complex was incubated in pH 7.4 MOPS-buffered solution for 1, 3, or 6 h at 37 °C. After these incubation periods, the aged solutions were diluted to 10 nM, and their mCa^{2+} uptake-inhibitory properties were determined. The transient curves of these experiments, showing the fluorescence response of the Calcium Green 5N sensor, demonstrate that mCa^{2+} uptake is increasingly impaired for complexes that were preincubated for longer time periods.

(Figure S25, SI). The normalized mCa^{2+} uptake rates plotted as a function of buffer preincubation time periods are shown in Figure 4. These data reveal all four carboxylate complexes to attain the same MCU-inhibitory activity as Ru265' after an incubation period of 6 h. These results suggest that axial ligand modification of Ru265 provides an effective means of generating aquation-activated prodrugs for Ru265'.

Intact Cell Mitochondrial Ca^{2+} Uptake Inhibition. Having demonstrated that 1–4 are active MCU inhibitors in permeabilized cells, we next sought to determine their ability to operate in intact cell systems like Ru265.⁴⁵ The mitochondria-localizing dye Rhod2AM was incubated with HeLa cells that were treated with 50 μ M of each complex for 1 h at 37 °C. Histamine was added to the cells to stimulate mitochondrial Ca^{2+} uptake, and the fluorescence response was measured and compared to nontreated cells. As was expected, Ru265 and the derivatives discussed in this work showed a decreased fluorescence response in comparison to untreated cells, as shown in Figure 5. These results demonstrate that these compounds maintain their potent MCU-inhibitory activity in intact cell systems.

CONCLUSIONS

In this work, four analogues of the potent MCU inhibitor Ru265 were described. These analogues, which contain axial carboxylate ligands, undergo aquation on the timescale of hours at 37 °C, releasing the diaqua-capped complex Ru265'. Importantly, we demonstrated that the intact carboxylate-capped species are less effective MCU inhibitors than Ru265', but upon aquation and formation of Ru265' they are equally potent. This result highlights that axial ligand modification

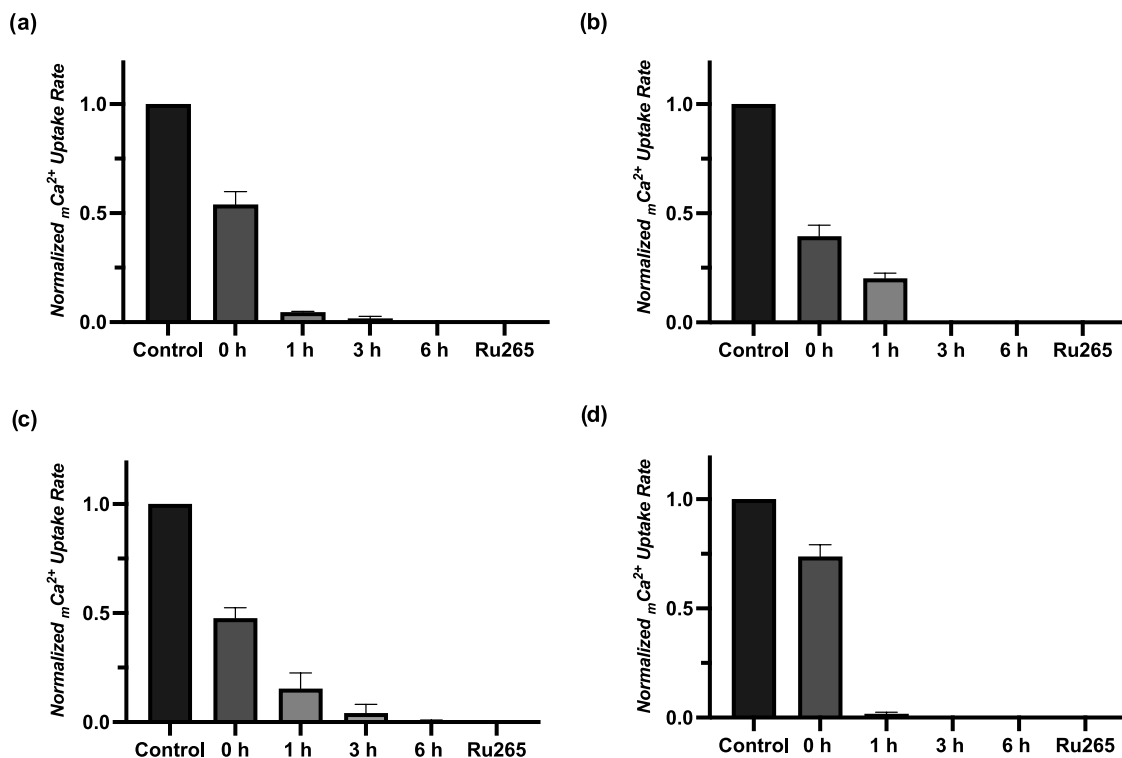


Figure 4. Time-dependent mitochondrial Ca^{2+} uptake rates within permeabilized HEK293T cells (1×10^7 cells mL^{-1}) treated with 10 nM solutions of (a) 1, (b) 2, (c) 3, and (d) 4 in pH 7.4 MOPS-buffered solution. Each time point was prepared from a 400 μ M stock of the complexes incubated in 40 mM MOPS-buffered solution (pH 7.4) and diluted to 10 nM in 18 $M\Omega$ -cm H_2O at the time of the experiment. All uptake rates were normalized to the rate of untreated (control) cells.

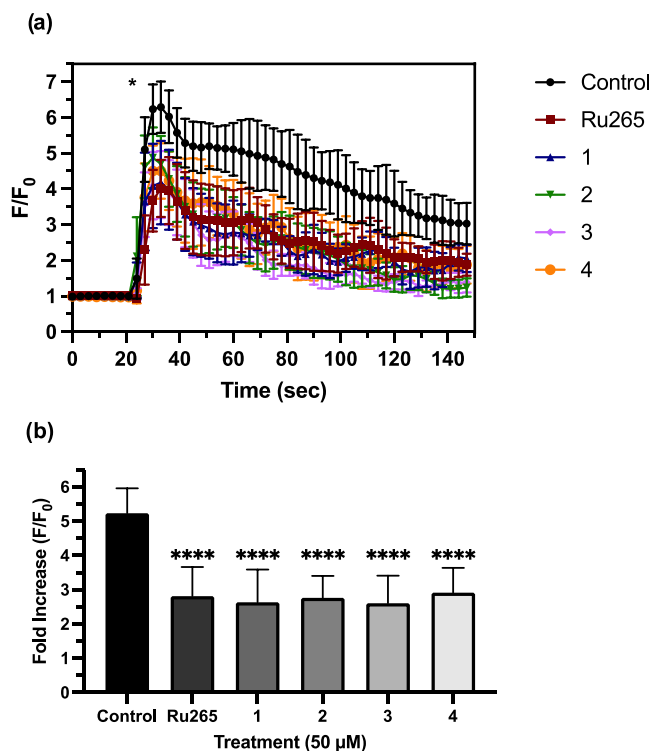


Figure 5. (a) Mitochondrial Ca^{2+} transients in HeLa cells after treatment with histamine ($100 \mu\text{M}$), indicated with an asterisk (*), that were pretreated with or without Ru265, 1, 2, 3, or 4 ($50 \mu\text{M}$) for 1 h. Data are presented as the mean response \pm SD. (b) Fold increase (F/F_0) of the fluorescence response of each treatment upon addition of histamine ($100 \mu\text{M}$). Data are presented as the mean response \pm SD. **** $p < 0.005$; $n = 6$.

represents a viable approach to develop prodrugs for Ru265'. The success of this strategy is important because we have previously shown that alteration of the equatorial ligands on the $\text{Ru}(\mu\text{-N})\text{Ru}$ core yields compounds that have significantly diminished or nonexistent MCU-inhibitory properties.^{45,51,82} Therefore, it appears that changes to the axial ligand represent the best strategy for fine-tuning the biological properties of this compound class without sacrificing the uptake and inhibitory efficacy. In addition, a comparison of the formate-capped complex 1 and the other alkyl carboxylate-capped complexes revealed the former to undergo aquation faster. Thus, the choice of appropriate axial ligands can have important impacts on the rate of prodrug activation, providing another means for modifying and optimizing compounds within this class for different biological applications. We envision that these studies will lay the groundwork for designing Ru265 analogues containing functional axial ligands with targeting capabilities or secondary biological activities. These types of modifications will allow for new more effective tools to study $m\text{Ca}^{2+}$ dynamics and potential therapeutic agents for the treatment of conditions that are mediated by $m\text{Ca}^{2+}$ dysregulation.

EXPERIMENTAL SECTION

Reagents and Materials. All reagents were obtained commercially and used without further purification. Ru265 was prepared as previously described.⁴⁵ Water ($18 \text{ M}\Omega\text{-cm}$) was purified using an ELGA PURELAB flex 2 (High Wycombe, U.K.).

Physical Measurements. 1D-NMR (^1H , $^{13}\text{C}\{^1\text{H}\}$, and ^{19}F) spectra were acquired at 25°C on a 500 MHz Bruker AV 3HD spectrometer equipped with a broadband Prodigy cryoprobe (Bruker,

Billerica, MA). Elemental analyses (C, H, N) were carried out by Atlantic Microlab Inc. (Norcross, GA). Fluorescence and absorbance of samples in 96-well plates were measured using a BioTek Synergy HT plate reader (Winooski, VT). GFAAS was performed using a PinAAcle 900Z spectrometer (PerkinElmer, Waltham, MA). Standardized solutions ($0\text{--}200 \mu\text{g L}^{-1}$) of ruthenium were used to generate a calibration curve. The concentrations of all ruthenium stock solutions applied in analytical and biological experiments were verified by GFAAS. Statistical analyses were performed using GraphPad Prism version 9.4.1 by applying a nonpaired student's *t*-test. Curve fitting was also performed using GraphPad Prism version 9.4.1 for Mac OS, GraphPad Software, San Diego, California.

Cell Lines and Culture Conditions. HeLa and HEK293T cells were obtained from American Type Culture Collection (ATCC, Washington DC) and cultured at 37°C as adherent monolayers in a humidified atmosphere containing 5% CO_2 in Dulbecco's modified Eagle's medium (DMEM) containing 4.5 g L^{-1} glucose, L-glutamine, and 3.7 g L^{-1} sodium bicarbonate supplemented with 10% fetal bovine serum (FBS). The cells were tested for mycoplasma contamination bimonthly through the commercial service provided by the College of Veterinary Medicine at Cornell University. All reagents and solutions used in biological studies were sterile-filtered through a $0.2 \mu\text{m}$ filter and maintained under sterile conditions.

Synthesis of $[(\text{HCO}_2)\text{Ru}(\text{NH}_3)_4(\mu\text{-N})\text{Ru}(\text{NH}_3)_4(\text{O}_2\text{CH})](\text{NO}_3)_3$ (1). Ru265 (100 mg, 0.189 mmol) was dissolved in 15 mL of $18 \text{ M}\Omega\text{-cm H}_2\text{O}$, and solid AgNO_3 (160 mg, 0.950 mmol; Alfa Aesar) was added to this solution. The reaction mixture was stirred at 50°C in the dark for 12 h. The resulting cloudy, orange suspension was filtered through celite to remove the precipitated AgCl . The orange filtrate was then treated with solid sodium formate (26 mg, 0.378 mmol; Fluka Chemical Corporation) and stirred at 50°C for 12 h. After cooling to room temperature, the orange solution was concentrated to dryness under vacuum, leaving an orange solid. This solid was dissolved in 1 mL of 10% formic acid in water. Orange crystals of the desired compound were obtained by the vapor diffusion of *p*-dioxane into this solution over the course of 3 days at room temperature. The mother liquor was decanted, and the remaining orange crystals were washed sequentially with 15 mL of ethanol, 15 mL of methanol, and 15 mL of acetone, before drying under vacuum. Yield: 29.7 mg (0.047 mmol, 25%). $^1\text{H NMR}$ (500 MHz, $\text{DMSO-}d_6$) δ (ppm) = 4.01 (s, 24H), 8.12 (s, 2H). $^{13}\text{C}\{^1\text{H}\}$ NMR (126 MHz, $\text{DMSO-}d_6$) δ (ppm) = 170.02. IR (ATR) ν (cm^{-1}) = 3295 (s, br), 1606 (m), 1384 (s), 1063 (m), 830 (m). Elemental analysis: calcd (% for $\text{C}_2\text{H}_{26}\text{N}_{12}\text{O}_{13}\text{Ru}_2 \cdot 3.5\text{H}_2\text{O}$) C 3.47; H 4.81; N 24.31. Found (%) C 3.74; H 4.72; N 24.11.

Synthesis of $[(\text{CH}_3\text{CO}_2)\text{Ru}(\text{NH}_3)_4(\mu\text{-N})\text{Ru}(\text{NH}_3)_4(\text{O}_2\text{CCH}_3)](\text{NO}_3)_3$ (2). The synthesis of 2 was carried out following the procedure described for 1, using the same quantities of Ru265 and AgNO_3 . In place of sodium formate, sodium acetate (31 mg, 0.378 mmol; Fluka Chemical Corporation) was used, and the crystallization employed 10% acetic acid instead of 10% formic acid. Yield: 26.0 mg (0.040 mmol, 21%). $^1\text{H NMR}$ (500 MHz, $\text{DMSO-}d_6$) δ (ppm) = 3.95 (s, 24H), 1.77 (s, 6H). $^{13}\text{C}\{^1\text{H}\}$ NMR (126 MHz, $\text{DMSO-}d_6$) δ (ppm) = 178.83, 24.94. IR (ATR) ν (cm^{-1}) = 3295 (s, br), 1575 (m), 1384 (s), 1040 (m), 830 (m). Elemental analysis: calcd (% for $\text{C}_4\text{H}_{30}\text{N}_{12}\text{O}_{13}\text{Ru}_2 \cdot \text{H}_2\text{O}$) C 7.12; H 4.78; N 24.92. Found (%) C 7.09; H 4.65; N 24.71.

Synthesis of $[(\text{CH}_3\text{CH}_2\text{CO}_2)\text{Ru}(\text{NH}_3)_4(\mu\text{-N})\text{Ru}(\text{NH}_3)_4(\text{O}_2\text{CCH}_2\text{CH}_3)](\text{NO}_3)_3$ (3). The synthesis of 3 was carried out following the procedure described for 1, using the same quantities of Ru265 and AgNO_3 . In place of sodium formate, sodium propionate (36 mg, 0.378 mmol; Alfa Aesar) was used, and the crystallization employed 10% propanoic acid instead of 10% formic acid. Yield: 18.1 mg (0.026 mmol, 14%). $^1\text{H NMR}$ (500 MHz, $\text{DMSO-}d_6$) δ (ppm) = 3.96 (s, 24H), 2.05 (q, 4H, $J = 7.5 \text{ Hz}$), 0.92 (t, 6H, $J = 7.5 \text{ Hz}$). $^{13}\text{C}\{^1\text{H}\}$ NMR (126 MHz, $\text{DMSO-}d_6$) δ (ppm) = 181.76, 30.33, 10.05. IR (ATR) ν (cm^{-1}) = 3295 (s, br), 1565 (m), 1384 (s), 1048 (m), 830 (m). Elemental analysis: calcd (% for $\text{C}_6\text{H}_{34}\text{N}_{12}\text{O}_{13}\text{Ru}_2 \cdot 1.5\text{H}_2\text{O}$) C 10.13; H 5.24; N 23.62. Found (%) C 10.09; H 4.81; N 23.72.

Synthesis of $[(CH_3(CH_2)_2CO_2)Ru(NH_3)_4(\mu-N)Ru(NH_3)_4(O_2C-CH_2)_2CH_3](OSO_2CF_3)_3$ (4). Ru265 (100 mg, 0.189 mmol) was dissolved in 15 mL of 18 M Ω -cm H₂O. Solid AgOSO₂CF₃ (243 mg, 0.950 mmol; Aldrich Chemical Company) was added, and the reaction mixture was stirred at reflux for 3 h in the dark. Insoluble AgCl was removed by filtration through celite, and sodium butyrate (41 mg, 0.378 mmol; Aldrich Chemical Company) was added to the orange filtrate, which was then stirred at 50 °C for 12 h. The orange solution was cooled to room temperature and concentrated to dryness under vacuum to yield an orange solid. This solid was dissolved in 1 mL of methanol and crystallized by allowing diethyl ether to vapor-diffuse into this solution at room temperature over the course of 2 days. The resulting orange crystals were washed sequentially with 15 mL of acetone and 15 mL of diethyl ether, and then dried under vacuum. Yield: 14.7 mg (0.015 mmol, 8%). ¹H NMR (500 MHz, DMSO-*d*₆) δ (ppm) = 3.92 (s, 24H), 2.01 (t, 4H, *J* = 7.5 Hz), 1.45 (q, 4H, *J* = 7.5 Hz), 0.83 (t, 6H, *J* = 7.5 Hz). ¹³C{¹H} NMR (126 MHz, DMSO-*d*₆) δ (ppm) = 181.80, 31.17, 19.22, 14.52. ¹⁹F NMR (470 MHz, DMSO-*d*₆) δ (ppm) = -77.75. IR (ATR) ν (cm⁻¹) = 3295 (m, br), 1603 (m), 1253 (s), 1170 (s), 1033 (m), 830 (w), 632 (m), 516 (w). Elemental analysis: calcd (% for C₁₁H₃₈N₉O₁₃F₉S₃Ru₂·CH₃OH) C 14.33; H 4.21; N 12.53. Found (%) C 14.09; H 4.28; N 12.30.

X-ray Crystallography. Single crystals of **3** were obtained via the vapor diffusion of *p*-dioxane into aqueous solutions of the compound in 10% propionic acid at room temperature. Compound **1** was converted to the triflate salt, and single crystals were obtained via vapor diffusion of diethyl ether into a methanolic solution of this compound at room temperature. Low-temperature X-ray diffraction data for **1** and **3** were collected on a Rigaku XtaLAB Synergy diffractometer coupled to a Rigaku Hypix detector with either Mo *K* α radiation (λ = 0.71073 Å) or Cu *K* α radiation (λ = 1.54184 Å), from PhotonJet micro-focus X-ray sources at 100 K. The diffraction images were processed and scaled using the CrysAlisPro software (Rigaku Oxford Diffraction, The Woodlands TX). The structures were solved through intrinsic phasing using SHELXT⁸³ and refined against *F*² on all data by full matrix least squares with SHELXL⁸⁴ following established refinement strategies.⁸⁵ All nonhydrogen atoms were refined anisotropically. All hydrogen atoms bound to carbon were included in the model at geometrically calculated positions and refined using a riding model. Hydrogen atoms bound to oxygen were located in the difference Fourier synthesis and subsequently refined semifreely with the help of distance restraints. The isotropic displacement parameters of all hydrogen atoms were fixed to 1.2 times the U_{eq} value of the atoms they are linked to (1.5 times for methyl groups). Details of the data quality and a summary of the residual values of the refinements are listed in Tables 1 and 2 and S1.

Compound **1** crystallized in the space group *P*2₁/*c*; the crystal is twinned and the structure was refined using an HKLF 5 file containing data for two twin domains, with a refined BASF of 0.1965(9). Within the asymmetric unit, two molecules of the complex cation were present, along with six triflate counterions and three methanol molecules. Two of the three methanol molecules were disordered about two distinct orientations and refined accordingly with appropriate similarity restraints, constraining the sum of the occupancy to be 1. Likewise, rotational and positional disorder was identified in three of the triflate counterions and was refined accordingly. Finally, one of the coordinated formate ligands was modeled as being disordered about two orientations. CheckCIF analysis of the structure of **1** reveals a B-level alert that arises from a short contact (2.70 Å) between atoms O1S and O8. O1S belongs to a methanol molecule present within the crystal lattice and O8 belongs to the noncoordinating formate ligand of one of the complex cations. This close contact is a consequence of a likely hydrogen-bonding interaction between these two molecules. The alert is triggered by the fact that the hydrogen atom of the methanol was not included in the refinement model because it could not be definitively located on the difference Fourier map.

NMR Kinetics Studies. Aqueous solutions were prepared to contain 400 μ M complex, 40 mM MOPS buffer (pH 7.4), 10% D₂O for NMR field-locking, and 0.1% *p*-dioxane as an internal reference (δ

= 3.75 ppm in D₂O). The aqution of complexes at 37 °C was monitored via the evolution of selected proton resonances arising from the carboxylate functional groups in the ¹H NMR spectra. The concentrations of the starting materials (**A**), monoaquated intermediates (**B**), and free ligands (**L**) were calculated using the relative integration of the corresponding proton resonances. Rate constants were calculated by fitting the concentration vs time data to the established integrated rate laws for consecutive reactions (eqs 1–5) using GraphPad Prism.

Cytotoxicity Assay. HeLa and HEK293T cells were seeded in 96-well plates with ~4000 cells/well and incubated overnight. On the following day, the culture media was removed, and cells were treated with media containing varying concentrations of the test complex and incubated for 72 h. The cells were then incubated in DMEM containing 1 mg mL⁻¹ MTT without FBS for 3 h. Following incubation, the media was removed, and the purple formazan crystals were dissolved in 200 μ L of an 8:1 dimethyl sulfoxide (DMSO)/glycine buffer (pH 10) mixture. The absorbance at 570 nm of each well was measured using a BioTek Synergy HT plate reader. The average absorbance of control cells was set to 100% viability, and the average absorbances of treated cells were normalized to the control absorbance. Data were plotted as percent viability versus the log[concentration]. The Hill Equation was applied to the data to determine the IC₅₀. Data are reported as the average of three independent biological replicates \pm SD.

Mitochondrial Membrane Potential via JC-1 Assay. Approximately 1 \times 10⁵ HeLa or HEK293T cells were seeded in 35 mm glass-bottom dishes (MatTek Life Sciences, Ashland, MA) and incubated overnight at 37 °C. On the next day, the cells were treated with the desired complex (50 μ M) and incubated for an additional 24 h at 37 °C. The culture media was then removed and replaced with fresh media supplemented with 10 μ M JC-1 dye, followed by incubation in the dark for 30 min at 37 °C. The dye-containing media was removed, and the cells were washed with 2 \times 1 mL phosphate-buffered saline (PBS, Corning Life Sciences). The cells were imaged in 1 mL of PBS. Control dishes were handled identically to treated dishes. For the positive control dishes, 50 μ M carbonyl cyanide *m*-chlorophenyl hydrazine (CCCP) in PBS was used, and the images were collected without the removal of CCCP. The cells were imaged using an EVOS M5000 fluorescence microscope (ThermoFisher, Waltham, MA) with a green fluorescence protein (GFP) filter cube (ex. 457–487/em. 502–538) for the green monomer fluorescence and a Texas red filter cube (ex. 542–582/em. 604–644) for the red J-aggregate fluorescence. The cellular images were analyzed using ImageJ (NIH) and the corrected total cellular fluorescence (CTCF) was calculated using the following formula

$$\text{CTCF} = \text{integrated density} - (\text{area of cell} \times \text{mean fluorescence of background reading})$$

For each replicate, the average red/green fluorescence was determined using at least eight independent cells and was normalized to untreated control cells ($[\text{red/green}]_{\text{control}} = 1$). Data are reported as the average of three independent trials \pm SD.

Cell Uptake. HeLa and HEK293T cells were grown to near confluence in six-well plates. On the day of the experiment, the culture media was removed, and the cells were treated with fresh media containing 0 or 50 μ M complex and incubated for 2 h at 37 °C. The culture media was then removed, and the adherent cells were washed with PBS, detached with 0.05% trypsin + 0.53 mM ethylenediaminetetraacetic acid (EDTA; Corning Life Sciences), and then pelleted by centrifugation (800g for 10 min). The cell pellet was suspended in ice-cold lysis buffer (1% w/v 3-[3-cholamidopropyl]dimethylammonio]-1-propanesulfonate (CHAPS), 5 mM EDTA, 50 mM tris(hydroxymethyl)aminomethane (Tris), and 100 mM NaCl; (pH 7.4). The suspension was vortexed for 30 s and incubated on ice for 45 min. The cell lysate was centrifuged to remove precipitated debris and the supernatant was transferred to a clean tube prior to analysis. The Ru content of the lysate was determined using GFAAS and was normalized to the protein content

of the sample, which was determined using the bicinchoninic acid (BCA) assay kit following manufacturer instructions (ThermoFisher). Results are reported as the average mass ratio of Ru to protein (pg/ μ g) in each sample \pm SD.

Role of OCT3 in Cellular Uptake. Approximately 1×10^5 HeLa cells were seeded in six-well plates and incubated at 37 °C overnight. On the next day, the culture media was removed, and the cells were treated with fresh media supplemented with the test complex (50 μ M) and the OCT3 inhibitor decynium-22 (1 μ M). The cells were incubated for 3 h before they were washed, harvested, lysed, and analyzed as described above. Results are reported as the average mass ratio of Ru to protein (pg/ μ g) in each sample \pm SD.

Mitochondrial Ca^{2+} Uptake in Permeabilized HEK293T Cells. HEK293T cells were grown to near confluency in a 10 cm^2 dish and harvested with trypsin. The cells were pelleted by centrifugation, suspended in cold PBS supplemented with 5 mM EDTA (pH 7.4), and counted using trypan blue. The cells were pelleted by centrifugation at 800g for 5 min and resuspended in ice-cold KCl solution (125 mM KCl, 20 mM 4-(2-hydroxyethyl)-1-piperazineethanesulfonic acid (HEPES), 2 mM K_2HPO_4 , 5 mM glutamate, 5 mM malate, 1 mM MgCl_2 , pH 7.2 with KOH) supplemented with 80 μ M digitonin and 1 μ M thapsigargin. The final solution contained < 0.1% DMSO, originating from the digitonin and thapsigargin stocks. The cells were incubated on ice for 15 min and centrifuged at 200g for 10 min at 4 °C. The pelleted cells were then resuspended in high KCl solution containing 1 μ M Calcium Green 5N (ThermoFisher, Waltham, MA) and 2 mM succinate to a final density of 1×10^7 cells/mL. For each experiment, 100 μ L of the cell suspension was placed in each well of a black-walled 96-well plate, treated with the desired concentration of the test complex, and allowed to equilibrate at room temperature for \sim 200 s. The background fluorescence of each well was recorded for 60 s prior to the addition of 20 μ M CaCl_2 . The change in fluorescence of the dye (ex. 488/em. 528) in response to Ca^{2+} was recorded every 5 s for at least 120 s or until the fluorescence returned to the baseline. The ${}_m\text{Ca}^{2+}$ uptake rate was calculated as the time constant in the exponential fit of the decay in fluorescence response curve. Control cells that were not treated with compound were handled identically to the treated cells to account for different incubation lengths. The Ca^{2+} uptake rate of treated cells was normalized to that of the control cells (0% inhibition), and each replicate was performed using independently prepared cell suspensions to account for differences in cell count. A BCA assay was performed on each cell suspension for every experiment, giving a protein content of \sim 1200 μ g mL^{-1} each time. The Hill equation was used to determine the IC_{50} of MCU inhibition. Data are presented as the average of three independent biological replicates \pm SD.

Time-Dependent Mitochondrial Ca^{2+} Uptake Experiments. Aqueous solutions of 400 μ M complex were prepared in 40 mM MOPS buffer (pH 7.4; 100-fold excess buffer). The solutions were incubated at 37 °C for 1, 3, and 6 h before being immediately frozen in liquid nitrogen. Each solution was stored at -80 °C until the ${}_m\text{Ca}^{2+}$ uptake experiments were performed. Each stock solution was then diluted in 18 M Ω -cm H_2O to a final concentration of 10 nM complex in the black-walled 96-well plates (200 nM complex before dilution with cell suspension). The ${}_m\text{Ca}^{2+}$ uptake assay was performed as described above with a concentration of 1×10^7 HEK293T cells/mL. Data were analyzed as described above and presented as the average ${}_m\text{Ca}^{2+}$ uptake rate of three independent biological replicates \pm SD.

Mitochondrial Ca^{2+} Uptake in Intact HeLa Cells Using Rhod2AM. Approximately 5×10^4 HeLa cells were seeded in an 8-well μ -slide (Ibidi USA, Inc., Fitchburg, WI) and incubated overnight at 37 °C. The following day, the cells were treated with the desired metal complex (50 μ M) in DMEM supplemented with 10% FBS for 1 h at 37 °C. The culture media was removed, and the cells were washed with 1×1 mL of PBS before the cells were incubated in extracellular medium (ECM; 135 mM NaCl, 20 mM HEPES, 5 mM KCl, 1 mM MgCl_2 , 1 mM CaCl_2) supplemented with 10 mM glucose, 3.2 mg mL^{-1} bovine serum albumin (BSA), 0.003% Pluronic F127, and 2 μ M Rhod2AM (Molecular Probes) in the dark for 30 min at

room temperature. The ECM was then removed, the cells were washed with 1×1 mL of ECM, and the cells were treated with fresh ECM supplemented with 10 mM glucose and 3.2 mg mL^{-1} BSA and incubated for an additional 30 min in the dark at room temperature. The buffer was then removed, and the cells were washed with 1×1 mL ECM and treated with ECM supplemented with 10 mM glucose and 3.2 mg mL^{-1} BSA. The cells were incubated for 15 min at 37 °C before imaging using a Zeiss LSM i710 confocal microscope using a 40 \times oil objective with an excitation of 561 nm and an emission window of 568–712 nm. After \sim 30 s of baseline recording, histamine (final concentration of 100 μ M) was added to the dish and fluorescence images were collected every 3 s to monitor ${}_m\text{Ca}^{2+}$ uptake. Images were analyzed and quantified using ImageJ and the CTCF was calculated. The average of at least six individual cells was used to determine the average CTCF for each replicate. Results are reported as the average of two independent replicates \pm SD.

■ ASSOCIATED CONTENT

Supporting Information

The Supporting Information is available free of charge at <https://pubs.acs.org/doi/10.1021/acs.inorgchem.2c02930>.

Complex characterization data including NMR and IR spectroscopy, and biological studies including cell viability curves, ${}_m\text{Ca}^{2+}$ uptake data, and cell stability studies (PDF)

Accession Codes

CCDC 2201612–2201613 contain the supplementary crystallographic data for this paper. These data can be obtained free of charge via www.ccdc.cam.ac.uk/data_request/cif, or by emailing data_request@ccdc.cam.ac.uk, or by contacting The Cambridge Crystallographic Data Centre, 12 Union Road, Cambridge CB2 1EZ, UK; fax: +44 1223 336033.

■ AUTHOR INFORMATION

Corresponding Author

Justin J. Wilson – Department of Chemistry and Chemical Biology, Cornell University, Ithaca, New York 14853, United States; orcid.org/0000-0002-4086-7982; Email: jjw275@cornell.edu

Authors

- Nicholas P. Bigham – Department of Chemistry and Chemical Biology, Cornell University, Ithaca, New York 14853, United States; orcid.org/0000-0001-9188-1453
- Zhouyang Huang – Department of Chemistry and Chemical Biology, Cornell University, Ithaca, New York 14853, United States; orcid.org/0000-0003-0335-2020
- Jesse Spivey – Department of Chemistry and Chemical Biology, Cornell University, Ithaca, New York 14853, United States
- Joshua J. Woods – Department of Chemistry and Chemical Biology, Cornell University, Ithaca, New York 14853, United States; Robert F. Smith School of Engineering, Cornell University, Ithaca, New York 14853, United States; Present Address: Chemical Sciences Division, Lawrence Berkeley National Laboratory, Berkeley, California 94720, United States; orcid.org/0000-0002-6213-4093
- Samantha N. MacMillan – Department of Chemistry and Chemical Biology, Cornell University, Ithaca, New York 14853, United States; Present Address: Department of Chemistry and Chemical Biology, Cornell University, Ithaca, New York 14853, United States; orcid.org/0000-0001-6516-1823

Complete contact information is available at:
<https://pubs.acs.org/10.1021/acs.inorgchem.2c02930>

Author Contributions

[§]Z.H. and J.S. contributed equally to this work.

Notes

The authors declare no competing financial interest.

ACKNOWLEDGMENTS

This research was supported by Cornell University, the United States National Science Foundation (NSF) under award number CHE-1750295, the Research Corporation for Science Advancement through a Cottrell Scholar Award, and the American Heart Association (AHA Predoctoral Fellowship to J. J. Woods; award no. 20PRE35120390). This work made use of the Cornell University NMR facility, which is supported by the NSF under award number CHE-1531632. Additional resources included the use of the Cornell University Biotechnology Resource Center, which is supported by the NIH (NIH S10RR025502).

REFERENCES

- (1) Pozzan, T.; Rizzuto, R.; Volpe, P.; Meldolesi, J. Molecular and Cellular Physiology of Intracellular Calcium Stores. *Physiol. Rev.* **1994**, *74*, 595–636.
- (2) Berridge, M. J.; Bootman, M. D.; Roderick, H. L. Calcium Signalling: Dynamics, Homeostasis and Remodelling. *Nat. Rev. Mol. Cell Biol.* **2003**, *4*, 517–529.
- (3) Clapham, D. E. Calcium Signaling. *Cell* **2007**, *131*, 1047–1058.
- (4) Carafoli, E.; Brini, M. Calcium Signalling and Disease: Molecular Pathology of Calcium. In *Subcellular Biochemistry*; Springer: New York, NY, 2007; Vol. 45, pp 481–506.
- (5) Orrenius, S.; Gogvadze, V.; Zhivotovsky, B. Calcium and Mitochondria in the Regulation of Cell Death. *Biochem. Biophys. Res. Commun.* **2015**, *460*, 72–81.
- (6) Celsi, F.; Pizzo, P.; Brini, M.; Leo, S.; Fotino, C.; Pinton, P.; Rizzuto, R. Mitochondria, Calcium and Cell Death: A Deadly Triad in Neurodegeneration. *Biochim. Biophys. Acta, Bioenerg.* **2009**, *1787*, 335–344.
- (7) Abeti, R.; Abramov, A. Y. Mitochondrial Ca²⁺ in Neurodegenerative Disorders. *Pharmacol. Res.* **2015**, *99*, 377–381.
- (8) Gustafsson, A. B.; Gottlieb, R. A. Heart Mitochondria: Gates of Life and Death. *Cardiovasc. Res.* **2007**, *77*, 334–343.
- (9) Santulli, G.; Xie, W.; Reiken, S. R.; Marks, A. R. Mitochondrial Calcium Overload Is a Key Determinant in Heart Failure. *Proc. Natl. Acad. Sci. U.S.A.* **2015**, *112*, 11389–11394.
- (10) Zhou, B.; Tian, R. Mitochondrial Dysfunction in Pathophysiology of Heart Failure. *J. Clin. Invest.* **2018**, *128*, 3716–3726.
- (11) Vultur, A.; Gibhardt, C. S.; Stanisz, H.; Bogeski, I. The Role of the Mitochondrial Calcium Uniporter (MCU) Complex in Cancer. *Pflug. Arch. Eur. J. Physiol.* **2018**, *470*, 1149–1163.
- (12) Delierneux, C.; Kouba, S.; Shanmughapriya, S.; Potier-Cartereau, M.; Trebak, M.; Hempel, N. Mitochondrial Calcium Regulation of Redox Signaling in Cancer. *Cells* **2020**, *9*, 432.
- (13) Rimessi, A.; Pozzato, C.; Carparelli, L.; Rossi, A.; Ranucci, S.; de Fino, I.; Cigana, C.; Talarico, A.; Wieckowski, M. R.; Ribeiro, C. M. P.; Trapella, C.; Rossi, G.; Cabrini, G.; Bragonzi, A.; Pinton, P. Pharmacological Modulation of Mitochondrial Calcium Uniporter Controls Lung Inflammation in Cystic Fibrosis. *Sci. Adv.* **2020**, *6*, eaax9093.
- (14) Rimessi, A.; Vitto, V. A. M.; Patergnani, S.; Pinton, P. Update on Calcium Signaling in Cystic Fibrosis Lung Disease. *Front. Pharmacol.* **2021**, *12*, 581645.
- (15) Halestrap, A. P. Calcium, Mitochondria and Reperfusion Injury: A Pore Way to Die. *Biochem. Soc. Trans.* **2006**, *34*, 232–237.
- (16) Shintani-Ishida, K.; Inui, M.; Yoshida, K. Ischemia-Reperfusion Induces Myocardial Infarction through Mitochondrial Ca²⁺ Overload. *J. Mol. Cell. Cardiol.* **2012**, *53*, 233–239.
- (17) Sanderson, T. H.; Reynolds, C. A.; Kumar, R.; Przyklenk, K.; Huttemann, M. Molecular Mechanisms of Ischemia-Reperfusion Injury in Brain: Pivotal Role of the Mitochondrial Membrane Potential in Reactive Oxygen Species Generation. *Mol. Neurobiol.* **2013**, *47*, 9–23.
- (18) Kirichok, Y.; Krapivinsky, G.; Clapham, D. E. The Mitochondrial Calcium Uniporter Is a Highly Selective Ion Channel. *Nature* **2004**, *427*, 360–364.
- (19) Baughman, J. M.; Perocchi, F.; Girgis, H. S.; Plovanich, M.; Belcher-Timme, C. A.; Sancak, Y.; Bao, X. R.; Strittmatter, L.; Goldberger, O.; Bogorad, R. L.; Kotliansky, V.; Mootha, V. K. Integrative Genomics Identifies MCU as an Essential Component of the Mitochondrial Calcium Uniporter. *Nature* **2011**, *476*, 341–345.
- (20) Rizzuto, R.; De Stefani, D.; Raffaello, A.; Mammucari, C. Mitochondria as Sensors and Regulators of Calcium Signalling. *Nat. Rev. Mol. Cell Biol.* **2012**, *13*, 566–578.
- (21) Kamer, K. J.; Mootha, V. K. The Molecular Era of the Mitochondrial Calcium Uniporter. *Nat. Rev. Mol. Cell Biol.* **2015**, *16*, 545–553.
- (22) Nemani, N.; Shanmughapriya, S.; Madesh, M. Molecular Regulation of MCU: Implications in Physiology and Disease. *Cell Calcium* **2018**, *74*, 86–93.
- (23) De Stefani, D.; Raffaello, A.; Teardo, E.; Szabó, I.; Rizzuto, R. A Forty-Kilodalton Protein of the Inner Membrane Is the Mitochondrial Calcium Uniporter. *Nature* **2011**, *476*, 336–340.
- (24) Oxenoid, K.; Dong, Y.; Cao, C.; Cui, T.; Sancak, Y.; Markhard, A. L.; Grabarek, Z.; Kong, L.; Liu, Z.; Ouyang, B.; Cong, Y.; Mootha, V. K.; Chou, J. J. Architecture of the Mitochondrial Calcium Uniporter. *Nature* **2016**, *533*, 269–273.
- (25) Fan, C.; Fan, M.; Orlando, B. J.; Fastman, N. M.; Zhang, J.; Xu, Y.; Chambers, M. G.; Xu, X.; Perry, K.; Liao, M.; Feng, L. X-Ray and Cryo-EM Structures of the Mitochondrial Calcium Uniporter. *Nature* **2018**, *559*, 575–579.
- (26) Baradaran, R.; Wang, C.; Siliciano, A. F.; Long, S. B. Cryo-EM Structures of Fungal and Metazoan Mitochondrial Calcium Uniporters. *Nature* **2018**, *559*, 580–584.
- (27) Nguyen, N. X.; Armache, J.-P.; Lee, C.; Yang, Y.; Zeng, W.; Mootha, V. K.; Cheng, Y.; Bai, X.-C.; Jiang, Y. Cryo-EM Structure of a Fungal Mitochondrial Calcium Uniporter. *Nature* **2018**, *559*, 570–574.
- (28) Fan, M.; Zhang, J.; Tsai, C.-W.; Orlando, B. J.; Rodriguez, M.; Xu, Y.; Liao, M.; Tsai, M.-F.; Feng, L. Structure and Mechanism of the Mitochondrial Ca²⁺ Uniporter Holocomplex. *Nature* **2020**, *582*, 129–133.
- (29) Wang, Y.; Nguyen, N. X.; She, J.; Zeng, W.; Yang, Y.; Bai, X.-C.; Jiang, Y. Structural Mechanism of EMRE-Dependent Gating of the Human Mitochondrial Calcium Uniporter. *Cell* **2019**, *177*, 1252–1261.
- (30) Vais, H.; Payne, R.; Paudel, U.; Li, C.; Foskett, J. K. Coupled Transmembrane Mechanisms Control MCU-Mediated Mitochondrial Ca²⁺ Uptake. *Proc. Natl. Acad. Sci. U.S.A.* **2020**, *117*, 21731–21739.
- (31) Wang, C.; Baradaran, R.; Long, S. B. Structure and Reconstitution of an MCU–EMRE Mitochondrial Ca²⁺ Uniporter Complex. *J. Mol. Biol.* **2020**, *432*, 5632–5648.
- (32) Zhuo, W.; Zhou, H.; Guo, R.; Yi, J.; Zhang, L.; Yu, L.; Sui, Y.; Zeng, W.; Wang, P.; Yang, M. Structure of Intact Human MCU Supercomplex with the Auxiliary MICU Subunits. *Protein Cell* **2021**, *12*, 220–229.
- (33) Woods, J. J.; Wilson, J. J. Inhibitors of the Mitochondrial Calcium Uniporter for the Treatment of Disease. *Curr. Opin. Chem. Biol.* **2020**, *55*, 9–18.
- (34) Santo-Domingo, J.; Vay, L.; Hernández-SanMiguel, E.; Lobatón, C. D.; Moreno, A.; Montero, M.; Alvarez, J. The Plasma Membrane Na⁺/Ca²⁺ Exchange Inhibitor KB-R7943 Is Also a Potent Inhibitor of the Mitochondrial Ca²⁺ Uniporter. *Br. J. Pharmacol.* **2007**, *151*, 647–654.

- (35) Thu, V. T.; Kim, H.-K.; Long, L. T.; Lee, S.-R.; Hanh, T. M.; Ko, T. H.; Heo, H.-J.; Kim, N.; Kim, S. H.; Ko, K. S.; Rhee, B. D.; Han, J. NecroX-5 Prevents Hypoxia/Reoxygenation Injury by Inhibiting the Mitochondrial Calcium Uniporter. *Cardiovasc. Res.* **2012**, *94*, 342–350.
- (36) Schwartz, J.; Holmuhamedov, E.; Zhang, X.; Lovelace, G. L.; Smith, C. D.; Lemasters, J. J. Minocycline and Doxycycline, but Not Other Tetracycline-Derived Compounds, Protect Liver Cells from Chemical Hypoxia and Ischemia/Reperfusion Injury by Inhibition of the Mitochondrial Calcium Uniporter. *Toxicol. Appl. Pharmacol.* **2013**, *273*, 172–179.
- (37) Arduino, D. M.; Wettmarshausen, J.; Vais, H.; Navas-Navarro, P.; Cheng, Y.; Leimpek, A.; Ma, Z.; Delrio-Lorenzo, A.; Giordano, A.; Garcia-Perez, C.; Médard, G.; Kuster, B.; García-Sancho, J.; Mokranjac, D.; Foskett, J. K.; Alonso, M. T.; Perocchi, F. Systematic Identification of MCU Modulators by Orthogonal Interspecies Chemical Screening. *Mol. Cell* **2017**, *67*, 711–723.
- (38) Kon, N.; Murakoshi, M.; Isobe, A.; Kagechika, K.; Miyoshi, N.; Nagayama, T. DS16570511 Is a Small-Molecule Inhibitor of the Mitochondrial Calcium Uniporter. *Cell Death Discovery* **2017**, *3*, 17045.
- (39) Di Marco, G.; Vallese, F.; Jourde, B.; Bergsdorf, C.; Sturlese, M.; De Mario, A.; Techer-Etienne, V.; Haasen, D.; Oberhauser, B.; Schleeper, S.; Minetti, G.; Moro, S.; Rizzuto, R.; De Stefani, D.; Fornaro, M.; Mammucari, C. A High-Throughput Screening Identifies MICU1 Targeting Compounds. *Cell Rep.* **2020**, *30*, 2321–2331.
- (40) De Mario, A.; Tosatto, A.; Hill, J. M.; Kriston-Vizi, J.; Ketteler, R.; Reane, D. V.; Cortopassi, G.; Szabadkai, G.; Rizzuto, R.; Mammucari, C. Identification and Functional Validation of FDA-Approved Positive and Negative Modulators of the Mitochondrial Calcium Uniporter. *Cell Rep.* **2021**, *35*, 109275.
- (41) Emerson, J.; Clarke, M. J.; Ying, W.-L.; Sanadi, D. R. The Component of “Ruthenium Red” Responsible for Inhibition of Mitochondrial Calcium Ion Transport. Spectra, Electrochemistry, and Aqueous Kinetics. Crystal Structure of μ -O-[(HCO₂)(NH₃)₄Ru]₂Cl₃. *J. Am. Chem. Soc.* **1993**, *115*, 11799–11805.
- (42) Matlib, M. A.; Zhou, Z.; Knight, S.; Ahmed, S.; Choi, K. M.; Krause-Bauer, J.; Phillips, R.; Altschuld, R.; Katsube, Y.; Sperelakis, N.; Bers, D. M. Oxygen-Bridged Dinuclear Ruthenium Amine Complex Specifically Inhibits Ca²⁺ Uptake into Mitochondria in Vitro and in Situ in Single Cardiac Myocytes. *J. Biol. Chem.* **1998**, *273*, 10223–10231.
- (43) Unitt, J. F.; Boden, K. L.; Wallace, A. V.; Ingall, A. H.; Coombs, M. E.; Ince, F. Novel Cobalt Complex Inhibitors of Mitochondrial Calcium Uptake. *Bioorg. Med. Chem.* **1999**, *7*, 1891–1896.
- (44) Nathan, S. R.; Pino, N. W.; Arduino, D. M.; Perocchi, F.; MacMillan, S. N.; Wilson, J. J. Synthetic Methods for the Preparation of a Functional Analogue of Ru360, a Potent Inhibitor of Mitochondrial Calcium Uptake. *Inorg. Chem.* **2017**, *56*, 3123–3126.
- (45) Woods, J. J.; Nemani, N.; Shanmughapriya, S.; Kumar, A.; Zhang, M.; Nathan, S. R.; Thomas, M.; Carvalho, E.; Ramachandran, K.; Srikantan, S.; Stathopoulos, P. B.; Wilson, J. J.; Madesh, M. A Selective and Cell-Permeable Mitochondrial Calcium Uniporter (MCU) Inhibitor Preserves Mitochondrial Bioenergetics after Hypoxia/Reoxygenation Injury. *ACS Cent. Sci.* **2019**, *5*, 153–166.
- (46) Woods, J. J.; Rodriguez, M. X.; Tsai, C.-W.; Tsai, M.-F.; Wilson, J. J. Cobalt Amine Complexes and Ru265 Interact with the DIME Region of the Mitochondrial Calcium Uniporter. *Chem. Commun.* **2021**, *57*, 6161–6164.
- (47) Cervinka, J.; Gobbo, A.; Biancalana, L.; Markova, L.; Novohradsky, V.; Guelfi, M.; Zacchini, S.; Kasparkova, J.; Brabec, V.; Marchetti, F. Ruthenium(II)–Tris-Pyrazolylmethane Complexes Inhibit Cancer Cell Growth by Disrupting Mitochondrial Calcium Homeostasis. *J. Med. Chem.* **2022**, *65*, 10567–10587.
- (48) Moore, C. L. Specific Inhibition of Mitochondrial Ca⁺⁺ Transport by Ruthenium Red. *Biochem. Biophys. Res. Commun.* **1971**, *42*, 298–305.
- (49) Broekemeier, K. M.; Krebsbach, R. J.; Pfeiffer, D. R. Inhibition of the Mitochondrial Ca²⁺ Uniporter by Pure and Impure Ruthenium Red. *Mol. Cell. Biochem.* **1994**, *139*, 33–40.
- (50) Ying, W.-L.; Emerson, J.; Clarke, M. J.; Sanadi, D. R. Inhibition of Mitochondrial Calcium Ion Transport by an Oxo-Bridged Dinuclear Ruthenium Ammine Complex. *Biochemistry* **1991**, *30*, 4949–4952.
- (51) Woods, J. J.; Lovett, J.; Lai, B.; Harris, H. H.; Wilson, J. J. Redox Stability Controls the Cellular Uptake and Activity of Ruthenium-Based Inhibitors of the Mitochondrial Calcium Uniporter (MCU). *Angew. Chem., Int. Ed.* **2020**, *59*, 6482–6491.
- (52) Novorolsky, R. J.; Nichols, M.; Kim, J. S.; Pavlov, E. V.; Woods, J. J.; Wilson, J. J.; Robertson, G. S. The Cell-Permeable Mitochondrial Calcium Uniporter Inhibitor Ru265 Preserves Cortical Neuron Respiration after Lethal Oxygen Glucose Deprivation and Reduces Hypoxic/Ischemic Brain Injury. *J. Cereb. Blood Flow Metab.* **2020**, *40*, 1172–1181.
- (53) Woods, J. J.; Spivey, J. A.; Wilson, J. J. A [¹H,¹⁵N] Heteronuclear Single Quantum Coherence NMR Study of the Solution Reactivity of the Ruthenium-Based Mitochondrial Calcium Uniporter Inhibitor Ru265. *Eur. J. Inorg. Chem.* **2022**, *2022*, e202100995.
- (54) Testa, B.; Crivori, P.; Reist, M.; Carrupt, P.-A. The Influence of Lipophilicity on the Pharmacokinetic Behavior of Drugs: Concepts and Examples. *Perspect. Drug Discovery Des.* **2000**, *19*, 179–211.
- (55) Leeson, P. D.; Davis, A. M. Time-Related Differences in the Physical Property Profiles of Oral Drugs. *J. Med. Chem.* **2004**, *47*, 6338–6348.
- (56) Leeson, P. D.; Springthorpe, B. The Influence of Drug-like Concepts on Decision-Making in Medicinal Chemistry. *Nat. Rev. Drug Discovery* **2007**, *6*, 881–890.
- (57) Hughes, J. D.; Blagg, J.; Price, D. A.; Bailey, S.; DeCrescenzo, G. A.; Devraj, R. V.; Ellsworth, E.; Fobian, Y. M.; Gibbs, M. E.; Gilles, R. W.; Greene, N.; Huang, E.; Krieger-Burke, T.; Loesel, J.; Wager, T.; Whiteley, L.; Zhang, Y. Physicochemical Drug Properties Associated with in Vivo Toxicological Outcomes. *Bioorg. Med. Chem. Lett.* **2008**, *18*, 4872–4875.
- (58) Waring, M. J. Defining Optimum Lipophilicity and Molecular Weight Ranges for Drug Candidates-Molecular Weight Dependent Lower LogD Limits Based on Permeability. *Bioorg. Med. Chem. Lett.* **2009**, *19*, 2844–2851.
- (59) Gleeson, M. P.; Hersey, A.; Montanari, D.; Overington, J. Probing the Links between in Vitro Potency, ADMET and Physicochemical Parameters. *Nat. Rev. Drug Discovery* **2011**, *10*, 197–208.
- (60) Liu, X.; Testa, B.; Fahr, A. Lipophilicity and Its Relationship with Passive Drug Permeation. *Pharm. Res.* **2011**, *28*, 962–977.
- (61) Johnson, T. W.; Gallego, R. A.; Edwards, M. P. Lipophilic Efficiency as an Important Metric in Drug Design. *J. Med. Chem.* **2018**, *61*, 6401–6420.
- (62) Johnstone, T. C.; Lippard, S. J. The Effect of Ligand Lipophilicity on the Nanoparticle Encapsulation of Pt(IV) Prodrugs. *Inorg. Chem.* **2013**, *52*, 9915–9920.
- (63) Zheng, Y.-R.; Suntharalingam, K.; Johnstone, T. C.; Yoo, H.; Lin, W.; Brooks, J. G.; Lippard, S. J. Pt(IV) Prodrugs Designed to Bind Non-Covalently to Human Serum Albumin for Drug Delivery. *J. Am. Chem. Soc.* **2014**, *136*, 8790–8798.
- (64) Awuah, S. G.; Zheng, Y.-R.; Bruno, P. M.; Hemann, M. T.; Lippard, S. J. A Pt(IV) Pro-Drug Preferentially Targets Indoleamine-2,3-Dioxygenase, Providing Enhanced Ovarian Cancer Immunotherapy. *J. Am. Chem. Soc.* **2015**, *137*, 14854–14857.
- (65) Abu Ammar, A.; Raveendran, R.; Gibson, D.; Nassar, T.; Benita, S. A Lipophilic Pt(IV) Oxaliplatin Derivative Enhances Antitumor Activity. *J. Med. Chem.* **2016**, *59*, 9035–9046.
- (66) Hallett, A. J.; Placet, E.; Prieux, R.; McCafferty, D.; Platts, J. A.; Lloyd, D.; Isaacs, M.; Hayes, A. J.; Coles, S. J.; Pitak, M. B.; Marchant, S.; Marriott, S. N.; Allemann, R. K.; Dervisi, A.; Fallis, I. A. Exploring the Cellular Uptake and Localisation of Phosphorescent Rhenium:

fac-Tricarbonyl Metallosurfactants as a Function of Lipophilicity. *Dalton Trans.* **2018**, *47*, 14241–14253.

(67) Konkankit, C. C.; Vaughn, B. A.; Huang, Z.; Boros, E.; Wilson, J. J. Systematically Altering the Lipophilicity of Rhenium(I) Tricarbonyl Anticancer Agents to Tune the Rate at Which They Induce Cell Death. *Dalton Trans.* **2020**, *49*, 16062–16066.

(68) Johnston, D. H.; Shriver, D. F. Vibrational Study of the Trifluoromethanesulfonate Anion: Unambiguous Assignment of the Asymmetric Stretching Modes. *Inorg. Chem.* **1993**, *32*, 1045–1047.

(69) Parsons, S.; Clegg, W. Crystal Structure Analysis Principles and Practice. In *Crystal Structure Analysis Principles and Practice*; Oxford University Press: New York, NY, 2009; p 211.

(70) Matteoli, U.; Menchi, G.; Bianchi, M.; Piacenti, F.; Ianelli, S.; Nardelli, M. Structure and Catalytic Activity of Phosphine-Substituted Ruthenium Carbonyl Carboxylates. *J. Organomet. Chem.* **1995**, *498*, 177–186.

(71) Malik, K. Z.; Robinson, S. D.; Steed, J. W. Ruthenium Carboxylate Complexes $[\text{Ru}(\text{O}_2\text{CR})_2(\text{H}_2\text{O})(\text{Me}_3\text{SO})_3]$ (R = Me, CF_3)-Synthesis and X-Ray Crystal Structures. *Polyhedron* **2000**, *19*, 1589–1592.

(72) Hiett, N. P.; Lynam, J. M.; Welby, C. E.; Whitwood, A. C. Ruthenium Carboxylate Complexes as Easily Prepared and Efficient Catalysts for the Synthesis of β -Oxopropyl Esters. *J. Organomet. Chem.* **2011**, *696*, 378–387.

(73) Carmona, D.; Viguri, F.; Lamata, M. P.; Ferrer, J.; Bardají, E.; Lahoz, F. J.; García-Orduña, P.; Oro, L. A. Ruthenium Amino Carboxylate Complexes as Asymmetric Hydrogen Transfer Catalysts. *Dalton Trans.* **2012**, *41*, 10298–10308.

(74) Jeschke, J.; Gäbler, C.; Korb, M.; Rüffer, T.; Lang, H. Ruthenium Carboxylate Complexes as Efficient Catalysts for the Addition of Carboxylic Acids to Propargylic Alcohols. *Eur. J. Inorg. Chem.* **2015**, *2015*, 2939–2947.

(75) Wilson, J. J.; Lippard, S. J. Synthesis, Characterization, and Cytotoxicity of Platinum(IV) Carbamate Complexes. *Inorg. Chem.* **2011**, *50*, 3103–3115.

(76) Gellene, G. I. Application of Kinetic Approximations to the $\text{A} \rightleftharpoons \text{B} \rightarrow \text{C}$ Reaction System. *J. Chem. Educ.* **1995**, *72*, 196–199.

(77) Verhaagh, S.; Schweifer, N.; Barlow, D. P.; Zwart, R. Cloning of the Mouse and Human Solute Carrier 22a3 (Slc22a3/SLC22A3) Identifies a Conserved Cluster of Three Organic Cation Transporters on Mouse Chromosome 17 and Human 6q26–Q27. *Genomics* **1999**, *55*, 209–218.

(78) Gründemann, D.; Schechinger, B.; Rappold, G. A.; Schömig, E. Molecular Identification of the Corticosterone-Sensitive Extraneuronal Catecholamine Transporter. *Nat. Neurosci.* **1998**, *1*, 349–351.

(79) Koepsell, H.; Lips, K.; Volk, C. Polyspecific Organic Cation Transporters: Structure, Function, Physiological Roles, and Biopharmaceutical Implications. *Pharm. Res.* **2007**, *24*, 1227–1251.

(80) Ogasawara, M.; Yamauchi, K.; Satoh, Y.-I.; Yamaji, R.; Inui, K.; Jonker, J. W.; Schinkel, A. H.; Maeyama, K. Recent Advances in Molecular Pharmacology of the Histamine Systems: Organic Cation Transporters as a Histamine Transporter and Histamine Metabolism. *J. Pharmacol. Sci.* **2006**, *101*, 24–30.

(81) Phillips, C. Fluorophore-Based Mitochondrial Ca^{2+} Uptake Assay. *Bio-Protoc.* **2018**, *8*, e2934.

(82) Urgiles, J.; Nathan, S. R.; MacMillan, S. N.; Wilson, J. J. Dinuclear Nitrido-Bridged Ruthenium Complexes Bearing Diimine Ligands. *Dalton Trans.* **2017**, *46*, 14256–14263.

(83) Sheldrick, G. M. A Short History of SHELX. *Acta Crystallogr., Sect. A: Found. Crystallogr.* **2008**, *64*, 112–122.

(84) Sheldrick, G. M. Crystal Structure Refinement with SHELXL. *Acta Crystallogr., Sect. C: Struct. Chem.* **2015**, *71*, 3–8.

(85) Müller, P. Practical Suggestions for Better Crystal Structures. *Crystallogr. Rev.* **2009**, *15*, 57–83.

Recommended by ACS

Impact of Coordination Mode and Ferrocene Functionalization on the Anticancer Activity of N-Heterocyclic Carbene Half-Sandwich Complexes

Kelvin K. H. Tong, Christian G. Hartinger, *et al.*

OCTOBER 14, 2022
INORGANIC CHEMISTRY

READ 

Dynamics of the Energy Transfer Process in Eu(III) Complexes Containing Polydentate Ligands Based on Pyridine, Quinoline, and Isoquinoline as Chromophoric A...

Albano N. Carneiro Neto, Fabio Piccinelli, *et al.*

OCTOBER 06, 2022
INORGANIC CHEMISTRY

READ 

Reactions of $\text{Tc}^{\text{I}}(\text{NO})$ and $\text{Tc}^{\text{V}}\text{N}$ Complexes with Alkynes and Alkynides

Moritz Johannes Ernst, Ulrich Abram, *et al.*

JULY 14, 2022
ORGANOMETALLICS

READ 

Synthesis and Photochemical Properties of Re(I) Tricarbonyl Complexes Bound to Thione and Thiazol-2-ylidene Ligands

Matthew J. Stout, Peter V. Simpson, *et al.*

AUGUST 24, 2020
ORGANOMETALLICS

READ 

Get More Suggestions >